Porous architected biomaterial for a tibial-knee implant with minimum bone resorption and bone-implant interface micromotion

Amirmohammad Rahimizadeh[1], Zahra Nourmohammadi[1], Sajad Arabnejad[2], Michael Tanzer[3], Damiano Pasini[1]*

[1]Department of Mechanical Engineering, McGill University, Montreal, Quebec, H3A0C3, Canada

[2]Department of Biomedical Engineering, University of Michigan, Ann Arbor, Michigan, 48109, USA

[3]Jo Miller Orthopaedic Research Laboratory, Division of Orthopaedics, McGill University, Montreal, Quebec, H3G1A4, Canada

[*]Corresponding Author: Mechanical Engineering Department, McGill University, Montreal, Quebec, H3A0C3, Canada. Phone: 514-398-6295, Fax: 514-398-7365, Email:

Damiano.pasini@mcgill.ca

Abstract

This investigation presents the numerical development of a fully porous tibial knee implant that is suggested to alleviate the clinical problems associated with current prostheses that are fully solid. A scheme combining multiscale mechanics and topology optimization is proposed to handle the homogenized analysis and property tailoring of the porous architecture with the aim of reducing the stiffness mismatch between the implant and surrounding bone. The outcome of applying this scheme is a graded lattice microarchitecture that can potentially offer the implant an improved degree of load bearing capacity while reducing concurrently bone resorption and interface micromotion. Asymptotic Homogenization theory is used to characterize the mechanics of its building block, a tetrahedron based unit cell, and the Soderberg fatigue criterion to represent the implant fatigue resistance under multiaxial physiological loadings. The numerical results suggest that the overall amount of bone resorption around the graded porous tibial stem is 26% lower than that around a conventional, commercially available, fully dense titanium implant of identical shape and size. In addition, an improved interface micromotion is observed along the tibial stem, with values at the tip of the stem as low as 17 μm during gait cycle and 22 μm for deep bend compared to a fully dense implant. This decrease in micromotion compared to that of an identical solid implant made of titanium can reasonably be expected to alleviate post-operative end of stem pain suffered by some patients undergoing surgery at the present time.

Keywords: Porous biomaterial, Tibial knee implant, Bone resorption, End-of-stem pain, Multiscale Mechanics, Topology optimization.

1.   Introduction

Knee replacement implants currently used in total knee arthroplasty (TKA) are generally made of a fully solid material, such as Titanium alloys and Cobalt chrome (CoCr) [1]. Despite their improved characteristics when compared to late 1970s implants, existing knee stems feature homogeneous properties that fail to fulfill the complete set of mechanobiological requirements they are subjected to [1]. One of these is the-end-of-stem pain, which is experienced by 7% of the patients undergoing primary TKA [2]. In revision surgery, despite the adoption of modified long stems, end-of-stem pain has been reported to affect as many as 19% of the patients [2]. The incidence of end-of-stem pain has been documented for both fully cementless and fully cemented stems with stable fixation such that 9% of patients with fully cemented stems suffer from end-of-stem pain [3-5]. Similarly, for patients receiving a press-fit, cementless stem, an incidence rate of 14% has been reported in the literature [6]. As an alternative, hybrid fixation of a stemmed tibial component has been proposed and has now become the standard of care. With this technique, the tibial plateau and the proximal metaphysis are cemented, whereas the stem is cementless and press-fit into the tibial diaphysis [7]. Nevertheless, although this type of fixation offers a lower failure rate, pain at the stem tip has been reported by patients with a stemmed tibial component with hybrid fixation [3, 7, 8]. The etiology of this pain is most commonly attributed to the severe interface micromotion that develops between the stem tip and the surrounding native bone, a problem that results from the elastic modulus mismatch existing between them [6]. Recent efforts to reduce the risk of end-of stem pain have included modification of the implant macrogeometry and use of advanced materials, such as composites and functionally graded solids [9-11]. Using advanced materials, an enhanced performance has been reported in tibiofemoral articulation [12, 13] and bone-implant interface. In a recent study, Completo et al. [14] postulated that fine-tuning the material properties of the tibial stem tip to make it mechanically similar to that of the surrounding cortical bone could reduce the incidence of post-operative pain. They found that a polyethylene tip lowered the strain at the distal end of the tibial stem, which could contribute to a reduction in the occurrence of end-of-stem pain. Despite these modest improvements in trying to eliminate end-of-stem pain in the proximal tibia, there has been no modification of the tibial implant that has successfully dealt with the modulus mismatch and micromotion that occurs between the stem and the surrounding tibial bone [6].

The second consequence of the elastic modulus mismatch between the tibial implant and the surrounding host bone is bone resorption secondary to stress shielding. The modulus mismatch between the tibial component and the host bone results in periprosthetic bone loss in both primary and revision TKA [15]. There are studies in the literature that have shown the potential of decreasing bone resorption by means of reducing the implant stiffness [6, 16-18]. A reduction in implant stiffness to the order of magnitude of the surrounding bone tissue has been achieved in implants that use either composite materials or porous solids with uniform porosity [10, 19, 20]. These attempts, however, have shown only partial success. Only recently the tailoring of porosity gradients in porous hip stems has been demonstrated effective in reducing bone resorption secondary to stress-shielding [21-24]. Stress shielding around a TKA can predispose to a subsequent periprosthetic fracture and decreases the amount and quality of bone at the time of revision surgery. The contribution of material properties to stress shielding in the proximal tibia was investigated in a computational study, where a homogenous distribution of elastic properties was designed to be tuned to the order of magnitude of the surrounding cancellous bone [25]. However, since the elastic properties were assumed constant within the implant, the amount of stress shielding could not be reduced to minimum and a global reduction of bone resorption could not be achieved at the distal stem

[20]. Tawkol [26] found that customizing the elastic modulus within the tibial tray could contribute to a 46% reduction in the stresses transferred to the implant, thus resulting in a lower bone resorption. This reduction can be achieved by varying the elastic modulus from 40 GPa at the top of the tray to 110 GPa downward. Other strategies that deal with the resolution of the modulus mismatch between standard titanium implants and the surrounding tibia involve the use of highly porous materials, such as tantalum foam [27]. Although its biocompatibility and high volumetric porosity can provide an exceptional degree of compliance, tantalum foam has a quasi-uniform distribution of pores which has limited capacity in minimizing bone resorption and interface micromotion simultaneously. Recently, porous implants featuring uniform porosity have been introduced with the aim of improving the performance of solid implants [19, 20, 28]. Despite encouraging results, these implants fall short in addressing post-operative complications, namely the concurrent reduction of bone resorption and interface micromotion. Elastic property tailoring in hip stems was recognized already in the 1990s as a promising mean to reduce bone resorption [29, 30]. Whereas those studies focus on the use of functionally graded solids, more recently porous materials with tailored cellular architecture have been proved successful in reducing bone resorption secondary to stress shielding, promoting bone ingrowth and providing implant stability [21-24, 31]. This strategy has been recently adopted to design a hip replacement implant that can facilitate osseointegration and concurrently minimize bone resorption and bone-implant interface failure [21-24]. While this work focused on the suppression of bone resorption in a hip implant, a similar strategy can be extended to deal with stress shielding and micromotion that occur in present day stemmed tibial implants used in TKA.

In this numeric investigation, we introduce a fully porous cementless stemmed tibial implant for primary and revision knee replacement that has a 3D cellular architecture tailored to concomitantly minimize interface micromotion and bone resorption, while satisfying clinical strength and fatigue requirements. Section 2 of this study presents a systematic methodology integrating multiscale mechanics and topology optimization to tailor the material properties of the knee implant. Section 3 describes the finite element model of the tibia and the prosthesis implanted into the tibia, while Section 4 details the calculation of the mechanical properties of the implant building block. In Section 5, we present the governing equations of a gradient-based topology optimization scheme that is used to optimally design the 3D architecture of the porous knee-implant. Finally, the performance of the proposed tibial knee implant, in particular its interface micromotion and bone resorption, is numerically assessed and compared to that of two baseline concepts, a fully solid one that is commercially available, and a fully porous tibial implant identical to the fully solid one, but with uniform distribution of pores.

2. Methodology

In this work, we present a fully porous architected biomaterial for a tibial knee implant, specifically a stemmed tibial component, with tailored properties and macro geometry identical to that of a commercially available tibial component, as explained in detail in the following section. Figure 1 briefly depicts the numeric strategy proposed here. The mechanical properties of the building block are expressed as a function of its relative density, and their optimal gradients are determined via topology optimization starting from the tissue properties of the tibial native bone of a patient.

The major aspects of the proposed methodology rest on the integration of multiscale solid mechanics and hierarchical optimal design of materials [32, 33], as briefly summarized in the steps below:

- CT scan data from a 38 year old male are used to create the numerical model of his tibial geometry and bone tissue properties.
- An open cell, a Tetrahedron-based topology, is selected to modularly build the interior architecture of the porous tibial stem. The high strength characteristics of this unit cell ensure a minimum level of fatigue and static resistance, as deemed necessary to resist the set of repetitive loads the knee is subjected to [31]. Asymptotic homogenization is used to calculate the elastic constants of the unit cell, with characteristic length much smaller than the implant, as a function of its relative density [34-38].
- A first trial uniform distribution of relative density is assigned to the implant and 3D finite element analysis is undertaken. From this analysis, the stress and displacement regime over the geometry of the prosthesis is obtained and used to formulate a multi constraint topology optimization problem. On the microscale, the stress distribution over the lattice architecture is retrieved and used to determine the implant safety factor (SF) under static and fatigue conditions.
- To minimize bone resorption and interface micromotion around the tibial stem, topology optimization is solved for maximum implant compliance. The problem is also subjected to a set of inequality and equality constraints, which include average porosity of the cellular implant, along with safety factors for first cycle and infinite fatigue life. Implant compliance is obtained from the calculation of the total strain energy of the implant. Implant displacements at each mesh element node along with unit cell homogenized properties are then used to build the macro stiffness tensor of each element. The gradient of the objective function is then obtained through partially taking the derivatives of the stiffness tensor components with respect to the relative density.

- The design variables are grouped in the vector, b, which collects the relative density of all elements and is updated via the standard optimality criterion. The optimization process continues until the attainment of the optimised distribution of relative density.

2.1.   Finite element model

The three-dimensional (3D) finite element (FE) model of the tibial fixation is constructed through CT images from the left tibiae of a 38 year old male with a body weight of 900 N, as shown in Figure 2. The properties of bone are assumed to be isotropic, a simplification that does not lead to a considerable difference from the results that consider bone as orthotropic [39, 40]. The effective Young's modulus of each element is obtained through the apparent density of the corresponding element. The Hounsfield values (HU) obtained through the CT images are used to determine the apparent density of bone by using a linear interpolation between HU and apparent density. As a result, the effective elastic properties of bone are expressed as a function of the apparent density [39, 41, 42]. The procedure followed to compute the mechanical properties of the tibia is detailed in **Appendix A**.

The macrogeometry of the stemmed tibial knee implant was taken from a NexGen component (Zimmer, Warsaw, IN) commercially available and made of solid titanium. The tibial dimensions were measured and the tibia was templated using NexGen templates to determine the appropriate size of the tibial component and the tibial stem. The component was sized to ensure the central portion of the tibial tray was externally rotated to lie over the medial 1/3 of the tibial tubercle while choosing the largest size

possible that would cover the proximal tibia, 10 mm below the articular surface, but did not overhang. The tibial stem was chosen to fill the proximal tibial diaphysis. An offset tibial stem was required to permit anatomic positioning of the tibial tray and ensure centralization of the stem. This resulted in using a size 5 NexGen stemmed tibial implant with a 4 mm offset 100 mm stem extension, creating in a 145 mm offset stem. These implants were CT scanned to create the parameters used in this study. The identical design was then used to convert the solid stemmed tibial implant into the optimized 3D porous implant here proposed.

Figure 3 shows the geometry of the intact and implanted bone along with the applied loads and boundary conditions. The distal end of the bone is fixed to avoid rigid body motion. As clinically recommended, the exterior of the implant stem is made of a thin shell that eases the implant removal during revision surgery. This ensures that in a postoperative situation no bone ingrowth occurs onto the stem, which is press fitted into the cortical bone. On the other hand, the implant tray is kept fully porous, and for this reason bone ingrowth can occur beneath it. To accurately capture interface stability, two distinct contact models are implemented in this work, one for the tray and one for the stem below. The tibial tray is assumed fully bonded to the underlying bone of the tibial plateau; this scenario represents the incidence of bone ingrowth onto the tray. One benefit of this choice is the reduction in the computational cost required for the stability analysis on a non-linear frictional contact model [43]. On the other hand, a frictionless contact is assumed for the tibial stem below the tray, where a thin solid shell covers the implant. This contact model represents the weak bonding between the smooth metal and the surrounding bone tissue [43, 44]. At the bone implant interface, face to face contact elements with appropriate mesh type are used with results that show interfacial micromotion at an average error of about 10μm [43]. The entire stem surface is selected as the target member and the inner bone surface is selected to be the contact member. The Augmented Lagrangian method, where contact penetration is present but controlled to some degree, is used in the contact formulation and contact tractions are monitored at the Gauss points. A contact stiffness of 1 is considered at the contact regions. The time step control is set to be automatic, where the contact behaviour is reviewed at the end of each substep to ensure that neither drastic change in contact status nor excessive penetration occurs.

Four different load cases corresponding to the 20%, 30%, 40% of the gait cycle and deep-knee bend are all studied. The system of loads reported in Table 1 and adopted in this work represents the daily physiological loads experienced by a human. Obtained from *in-vivo* measurements on an instrumented knee joint, those values pertain to a subject with a male body weight of 1000N and provide contact load measures with an error below 2% [45-47]. The values in Table 1 are used with equal weights to calculate an equivalent load pattern that represents concurrently walking and deep knee bend, and is here used for the implant design.

2.2.   Homogenized mechanical properties
Mechanics and optimization of implant microarchitecture are here undertaken by treating the implant as a homogenized continuum, an assumption that allows to avoid detailed finite element simulations, which would be extensive and lengthy to handle [48]. By doing so, we can focus on a representative volume element (RVE) of the implant, and consider its properties as those of a homogenized medium equivalent to the implant itself. Below is a description of the method used in this paper to calculate the stiffness

tensor and implant fatigue resistance, which both depend on multiscale properties, specified at the macro and micro scale.

2.2.1. Elastic properties of unit cell

To obtain homogenized properties of the implant, we use asymptotic homogenization (AH) theory, which enables to calculate the stress and strain distribution developed within the cellular architecture, namely microstrain and microstress, from which the implant stiffness tensor can be obtained. The yield and ultimate strength of the lattice material are also assessed for relative density $\rho \leq 0.3$ and used to capture the fatigue strength of the designed implant via the Soderberg fatigue criterion under multi axial stresses [49].

The effective properties of the building block E_{ijkl}^{H} are obtained by solving a local problem formulated on the RVE and defined as [50]:

$$E_{ijkl}^{H} = \frac{1}{|Y|} \int_{Y_C} E_{ijpm} M_{pmkl} dY \tag{1}$$

where $|Y|$ is the unit cell volume, E_{ijpm} is the positional elastic tensor of the unit cell that varies between zero and the material elastic tensor corresponding to the voids and bulk material respectively. Furthermore, we define a structure tensor M_{pmkl} that relates the local macro strains $\overline{\varepsilon}_{kl}$ to the micro strains as

$$\varepsilon_{ij} = M_{ijkl}\overline{\varepsilon}_{kl} \tag{2a}$$

$$M_{ijkl} = \frac{1}{2}(\delta_{ik}\delta_{jl} + \delta_{il}\delta_{jk}) - \varepsilon_{ij}^{*kl} \tag{2b}$$

Where δ_{ij} is the Kronecker ς, and ε_{ij}^{*kl} is the microscopic strain corresponding to the component kl of the macroscopic strain. Given that for this application small deformation and linear elasticity hold, the microscopic strain ε_{ij}^{*kl} can be expressed as

$$\int_{Y_C} E_{ijpm} \varepsilon_{ij}^{1}(v) \varepsilon_{pm}^{*kl}(u) dY = \int_{Y_C} E_{ijkl} \varepsilon_{ij}^{1}(v) \overline{\varepsilon}_{kl} dY \tag{3}$$

where $\varepsilon_{ij}^{1}(v)$ denotes the virtual strain.

In three dimensions, six arbitrary macroscopic unit strains are required to construct the M_{ijkl} matrix. The periodicity of the strain field is ensured by imposing periodic boundary conditions on the RVE edges [50, 51]. As a result, the nodes of the opposite planes are set with identical displacement. Once the structure tensor, M_{ijkl}, is obtained, the homogenized stiffness tensor of the unit cell can be predicted by substituting the structure tensor M_{pmkl} into (2). The microscopic stress distribution, σ_{ij}, can be defined by

$$\sigma_{ij} = E_{ijkl} M_{klmn} \overline{\varepsilon}_{mn} \tag{4}$$

Using the microscopic stress tensor and introducing the homogenized elastic tensor, E_{rsmn}^H, results in a simplified relationship between the microscopic stress distribution and the macroscopic stress tensor

$$\sigma_{ij} = E_{ijkl} \, M_{klmn} \, (E_{rsmn}^H)^{-1} \bar{\sigma}_{rs} \tag{5}$$

wherein $\bar{\sigma}_{rs}$ is the macroscopic stress distribution applied to the RVE. If σ_{ys} is the yield strength of the cell walls, then the yield surface of the unit cell can be written from (5) as

$$\bar{\sigma}_{ij}^y = \frac{\sigma_{ys}}{\max\{\sigma_{VM}(\bar{\sigma}_{ij})\}} \bar{\sigma}_{ij} \tag{6}$$

where $\sigma_{VM}(\bar{\sigma}_{ij})$ is the von-Mises stress distribution within the unit cell caused by the applied macroscopic stress $\bar{\sigma}_{ij}$.

Figure 4 illustrates the predicted elastic moduli and yield strength of the unit cell used in this work for the tibial knee-implant, obtained for the generic case of multi axial loadings. A relative density ranging $0.05 < \rho < 1$ can be considered for the unit cell; however, since the cell topology degenerates for $\rho > 0.8$, we consider values of ρ between 0.05 and 0.8 only.

2.2.2. Fatigue properties

Implant stiffness tailoring is undertaken against high cycle fatigue failure such that stress values generated within the material architecture do not exceed the yield strength of Ti6A14V, the material the implant is made of. Hence, to obtain the fatigue surface $\bar{\sigma}_{ij}^e$ of the RVE, we multiply the RVE yield strength $\bar{\sigma}_{ij}^y$ by the ratio of the endurance limit σ_{es} and yield strength σ_{ys} of the solid material. This gives

$$\bar{\sigma}_{ij}^e = \bar{\sigma}_{ij}^y \frac{\sigma_{es}}{\sigma_{ys}} \tag{7}$$

Once the fatigue surface is obtained, the Soderberg diagram, a conservative criterion, can be constructed to compute the fatigue safety factor, $SF_{Fatigue}$, from the relation:

$$\frac{\bar{\sigma}_{ij}^m}{\bar{\sigma}_{ij}^y} + \frac{\bar{\sigma}_{ij}^a}{\bar{\sigma}_{ij}^e} = \frac{1}{SF_{Fatigue}} \tag{8}$$

wherein, $\bar{\sigma}_{ij}^m$ and $\bar{\sigma}_{ij}^a$ denote the mean and alternating stresses respectively, given by:

$$\bar{\sigma}_{ij}^m = \frac{\bar{\sigma}_{ij}^{\max} + \bar{\sigma}_{ij}^{\min}}{2} \tag{9a}$$

$$\bar{\sigma}_{ij}^a = \frac{\bar{\sigma}_{ij}^{\max} - \bar{\sigma}_{ij}^{\min}}{2} \tag{9b}$$

With $\bar{\sigma}_{ij}^{max}$ and $\bar{\sigma}_{ij}^{min}$ being the multiaxial macroscopic stresses that cause, respectively, the highest and the lowest von-Mises stress within the unit cell. From eq. (7) and (8), the static safety factor of the RVE is expressed as:

$$SF_{static} = \frac{\bar{\sigma}_{ij}^{y}}{\sigma_{ij}} \tag{10}$$

The procedure above is used for the analysis of the tibia knee implant which is modelled with homogenized properties representing the tetrahedron-based cell made of Ti6Al4V [52]. The properties of Ti6Al4V here adopted (Young's modulus: 120GPa, Poisson's ratio: 0.3, yield strength: 900MPa, fatigue strength: 600MPa at 10^{7}cycles) are measured from mechanical testing of 3d-printed samples manufactured via Selective Laser Melting [53]. SLM is the additive process that will be used for implant fabrication. In this work, we rely on the assumption that defects and imperfections emerging from the manufacturing process would not severely impact the mechanical properties [24, 31]. Further work, currently undergoing, is required to include the influence of manufacturing deviations in the implant analysis.

3.   Optimization scheme

A density-based topology optimization is here adopted to optimally tailor the material distribution in the stem of the tibial component [54]. The search for optimized density gradients is undertaken on an equivalent medium with homogenized properties obtained in section 2.2.1 and expressed as a function of relative density (Figure 4). A penalization scheme that penalizes elements with intermediate density values is used to create an implant with continuous density distribution [55].

3.1.   Problem formulation

Elastic stiffness tailoring aims at reducing the elastic modulus mismatch between implant microstructure and native bone, resulting in lower bone resorption. As such, to minimize bone-stem interface micromotion and bone resorption, the optimization problem is posed for minimum stiffness, which is equivalent to maximize implant compliance [56], here expressed as

$$c(\tilde{x}) = F^{T}U(\tilde{x}) \tag{11}$$

where F is the vector of the nodal forces applied to the implant and $U(\tilde{x})$ is the vector of nodal displacement. F can be expressed as

$$F = K(\tilde{x})U(\tilde{x}) \tag{12}$$

where $K(\tilde{x})$ is the total stiffness matrix of the implant [57]. The problem is subjected to multiple constraints, e.g. on volume, density, and safety factor, and can be formally formulated as:

$$
\begin{aligned}
&Find && x = [x_1, x_2,..., x_e,..., x_n] \\
&Maximize && c(\tilde{x}) = F^{T}U(\tilde{x}) \\
&subject\ to && v(\tilde{x}) = \tilde{x}^{T}v - \tilde{v} \leq 0 \\
&&& x \in \chi \quad \chi = \{x \in \mathbb{R}^{n} : x_{min} \leq x \leq x_{max}\} \\
&&& SF_{min} < SF
\end{aligned}
\tag{13}
$$

where $\tilde{x}$ is the density vector which is filtered through a basic filter function described in **Appendix B,** n is the total number of the elements that discretizes the implant domain, $V =[v_1,...,v_n]$ is the vector of the elements volume and $\tilde{v}$ is a prescribed volume of the tibial knee implant.

The optimization problem defined in (13) can be reformulated as a traditional problem of minimization by multiplying the objective function by -1, which results in

$$
\begin{aligned}
&Find && x = [x_1, x_2,..., x_e,..., x_n] \\
&Minimize && c(\tilde{x}) = -F^T U(\tilde{x}) \\
&subject\ to && v(\tilde{x}) = \tilde{x}^T v - \tilde{v} \leq 0 \\
& && x \in \chi \quad \chi = \{x \in \mathbb{R}^n : x_{min} \leq x \leq x_{max}\} \\
& && SF_{min} < SF
\end{aligned}
\tag{14}
$$

The derivative of the objective function can be determined as:

$$
\frac{\partial c(\tilde{x})}{\partial x_e} = \sum_{i \in N_e} \frac{\partial c(\tilde{x})}{\partial \tilde{x}_i} \frac{\partial \tilde{x}_i}{\partial x_e}
\tag{15}
$$

where $\tilde{x}_i$ represent the filtered density of element i and $\dfrac{\partial \tilde{x}_i}{\partial x_e}$ is defined by

$$
\frac{\partial \tilde{x}_i}{\partial x_e} = \frac{H_{ie} v_e}{\sum_{j \in N_i} H_{ij} v_j}
\tag{16}
$$

where H_{ij} is a weight factor matrix as described in **Appendix B**. From (11), $\dfrac{\partial c(\tilde{x})}{\partial \tilde{x}_i}$ can be defined by

$$
\frac{\partial c(\tilde{x})}{\partial \tilde{x}_i} = -F^T \frac{\partial U(\tilde{x})}{\partial \tilde{x}_i} = -U^T(\tilde{x}) K(\tilde{x}) \frac{\partial U(\tilde{x})}{\partial \tilde{x}_i}
\tag{17}
$$

where F^T and $U^T(\tilde{x})$ indicate the transpose matrix of F and $U(\tilde{x})$ respectively. Taking the derivative of (12) with respect to $\tilde{x}_i$ yields

$$
\frac{\partial K(\tilde{x})}{\partial \tilde{x}_i} U(\tilde{x}) + K(\tilde{x}) \frac{\partial U(\tilde{x})}{\partial \tilde{x}_i} = 0
\tag{18}
$$

As a result, $\dfrac{\partial U(\tilde{x})}{\partial \tilde{x}_i}$ can be expressed as follows:

$$
\frac{\partial U(\tilde{x})}{\partial \tilde{x}_i} = -K(\tilde{x})^{-1} \frac{\partial K(\tilde{x})}{\partial \tilde{x}_i} U(\tilde{x})
\tag{19}
$$

From (17) and (19), we can obtain the derivative of the objective function as

$$\frac{\partial c(\tilde{x})}{\partial \tilde{x}_i} = U(\tilde{x})^T \frac{\partial K(\tilde{x})}{\partial \tilde{x}_i} U(\tilde{x}) \qquad (20)$$

The procedure followed to calculate the derivative of the stiffness matrix of the implant microstructure with respect to the design variables is given in **Appendix C**. Once the sensitivity of the objective function is obtained, the design variables are updated using the standard optimality criterion (OC) scheme [58] until convergence is reached, as described in **Appendix D**.

4.   Results and Discussion

The methodology described in section 2 is here applied for the design of a fully porous knee implant. Two sets of numeric results are herein presented. The first describes the micro-architecture of the proposed tibial implant, and the second its performance, namely bone resorption and bone-stem interface micromotion, which are then compared to those of the fully solid titanium tibial implant and a fully porous one with uniform relative density.

4.1.   Implant architecture

Figure 5 shows the von Mises distribution and optimal density distribution of the microstructure of the proposed tibial implant which features low porosity at the distal region where severe stresses are located. As can be observed, stress concentration appears beneath the tray due to the variation in implant macrogeometry. In addition, the applied moment in the frontal plane, which represents the Varus-Valgus movement of knee joint, leads to high stress values at the distal region. The tibial implant is fully porous with very low porosity in the tibial tray. In particular, unit cells with high value of relative density ranging 0.7-0.8 are located at regions with high stress in the tibial tray, which ensures a minimum level of fatigue resistance. Hence, underneath the tray as well as in the lower part of the stem, cells with high relative density are necessary to meet the level of fatigue resistance the implant should provide.

From the relative density distribution, the lattice microarchitecture is created through in-house mapping scripts. Figure 5 shows that while the implant internal architecture is fully porous, a very thin shell is placed on the exterior of the stem only. This feature is designed to avoid bone ingrowth onto the stem and thus facilitate the process of implant replacement at the time of revision surgery. While the fully solid tibial implant shows fatigue strength 2 times higher than the cellular tibial implant, the latter has a safety factor of 3, which is well within the margin of safety for a biomedical device [59]. If a further increase in the implant fatigue strength is desired, either a lattice with smooth cell geometry could be implemented [49], or other part of the implant could be designed as fully dense.

4.2.   Implant micromotion

The primary stability of the implant is crucial to the success of the total knee arthroplasty (TKA) [60]. An extensive body of the literature has demonstrated that the elastic modulus mismatch from the bone tissue to the implant is one main cause of the lack of stability at the bone-implant interface [6, 14]. Although other factors such as the implant macrogeometry, the fixation technique used at the bone-implant interface, and the design platform of the implant play an important role in the development of interface micromotion [14, 60, 61], in this work we address the elastic modulus mismatch. To do so, we perform a relative comparison between implants that share identical macrogeometry and prescribed clinical conditions, such as the fixation type at the bone implant interface. The differences in interfacial

micromotion that we observe are therefore relative, and can be exclusively attributed to the distribution of elastic modulus that each tibial implant here examined features.

Figure 6 and 7 illustrate the distribution of bone-stem interface micromotion at 30% of gait cycle and deep bend, respectively. The amount of micromotion is computed from the relative nodal sliding distance of mesh elements from bone and stem. Stable fixation at the bone-stem interface with micromotion between 20 – 50 μm provides a desirable range, since this degree of micromotion is known to be well tolerated by the periprosthetic bone, and in cases of porous implants, is associated with bone ingrowth (Chong et al 2010). This range of micromotion can also contribute to a notable reduction of the end-of-stem pain that arises from excessive interface micromotion. The percentage of surface area (SA) with micromotion below $50 \mu m$ is then assessed for the designed graded lattice implant and the two baselines, a fully dense tibial implant and a uniform porosity tibial implant, all made of Ti6Al4V.

Both the loading conditions of gait cycle and deep knee bend led to severe micromotion around the distal part of the stem, particularly around the tip of the stem. High values of micromotion can cause the patient to feel pain at this region. At 30% of gait cycle, the graded lattice tibial implant stem resulted in a maximum micromotion at the stem tip that is reduced by 17μm and 10μm when compared respectively to a fully solid and a uniform lattice tibial implant stem. Although the maximum micromotion is reduced by only 15% when compared to a fully solid implant, from a clinical point of view this result suggests a lower potential for postoperative end-of-stem pain in patients. As can be seen, the surface area with micromotion below 50μm for the graded tibial implant (grey regions of the implant in Figure 6c) is larger than that of the two other implants (Figure 6a and 6b). This value of micromotion ensures an improved stability between the tray periphery and the distal part of the stem. During deep knee bend, a reduction in micromotion of the tip of the stem of 22 μm and 14 μm with respect to a fully dense titanium tibial implant and uniform porosity tibial implant were achieved. This amount represents a 14% reduction in the maximum micromotion at the stem tip for the graded lattice implant compared to the traditional solid implant. This provides the graded tibial implant with 76% prosthesis area with micromotion below 50 μm, values that are clinically stable.

Among the nodal displacement vectors, we now examine the displacement distribution at the mid (i) and distal areas (ii) of the implant, and plot the results in Figure 8. Here, is the micromotion distribution visualized for the loading conditions of walking and deep bend. 50 points around the stem surface have been specified with the first one located at the anterior of the cross section and the remaining ones following a counter clockwise direction. The figure shows the relative sliding micromotion values with respect to the fully solid implant for deep bend and 30% of gait cycle. As can be seen, maximum micromotion occurs anteriorly for both loading conditions. The interface micromotion for the graded lattice implant is lower relative to both baseline implants at almost all the points. Although the relative reduction is small, this result offers a lower probability of local interface failure and end-of stem pain.

4.3. Bone resorption

To further investigate the improved performance of the implant here introduced, we compute its amount of bone loss and compare to that of a fully dense and a uniform porosity tibial implants (ρ = 60%). Figure 9 shows the results with bone resorption levels plotted around the tibial stems in the three cases. The results are obtained by computing the amount of underloaded bone [21-24]. In particular, bone is assumed to start loosing its mass when the local strain energy (U_i) per unit of bone mass (ρ) averaged

over (n) loading cases $(S = ((1/n)\sum_{i=1}^{n} U_i / \rho))$ in the postoperative situation is beneath the respective local strain energy of the implant preoperatively $(S < (1-s)S_{ref})$. S_{ref} indicates the local strain energy of the intact bone and s indicates a specialized threshold level or dead-zone for the bone to start degrading after implantation. As a result, the amount of resorbed bone mass can be expressed as

$$m_r(b) = \frac{1}{M}\int_V g(S(b))\rho dV \tag{21}$$

where M and V are the mass and volume of the original bone and $g(S(b))$ is a resorptive function equal to unity if $S < (1-s)S_{ref}$ and otherwise is equal to zero. The value considered in this study for the dead-zone is 0.75 [29].

We observed that the computed amount of resorbed bone was consistent with the bone-stem stability. The less the bone-stem interface micromotion, the lower bone resorption. As can be seen, significant bone resorption appears proximally underneath the tray throughout the medial compartment of the tibia and propagates toward the lateral part. The concentration of bone resorption in the medial compartment can be attributed to the Varus-Valgus movement of the knee joint which causes a larger portion of the vertical load to be distributed over the medial part of the tibiae.

In Figure 10, we compare the amount of bone resorption at four different regions of the implanted tibia. As previously described, bone resorption is maximum at the proximal region, whereas at the distal regions an overstressed bone results in bone formation [62]. For the solid titanium stem, an overall bone resorption of 40% can be predicted with the greatest degree of resorption occurring in zone 3. Due to the higher compliance of the uniform lattice tibial implant, we observe an overall decrease of resorbed bone of 16%, i.e. two times lower than the solid tibial implant. The least amount of bone resorption was seen around the graded cellular implant, with an overall decrease of 26%, 3 times less than that seen around the solid tibial implant. In summary with respect to the fully solid baseline tibial knee implant, Figure 10 shows a reduction of bone resorption around the graded lattice tibial implant of 50 % at zone 4, 76% at zone 3 54% at zone 2, and 18% at zone 1.

Recent technologies for additive manufacturing (AM), such as electron beam melting (EBM) and selective laser melting (SLM), bring versatile layer-by-layer processes that enable the fabrication of porous materials with tailored cellular architecture [63]. For example, SLM, a powder bed fusion technology, has been used to generate parts with improved mechanical, tribological and corrosion properties [64]. Recent works have demonstrated that AM can successfully build metallic lattice structures including porous implants with complex internal microarchitecture [63, 65-69]. In addition, AM facilitates the fabrication of cellular implants with tailored gradients of porosity and pore morphology that enables bone ingrowth [70, 71]. A fully porous hip implant featuring a lattice microstructure similar to the one presented in this paper has been recently manufactured through SLM and successfully tested in vitro [24]. Its graded microarchitecture features a minimum strut thickness of 200μm and a maximum pore size of 800μm, characteristics that are built through AM and are shared by the knee implant presented in this study [31, 63]. These previous works therefore demonstrate the feasibility of additively manufacturing the knee implant architecture herein reported.

Exploratory in nature, this numeric study holds some limitations that need to be addressed in the future. The first one is that a simplified loading system representing a high body weight has been used to perform the numerical analysis. Although this system of loadings describes the worst-case scenario that can occur during normal daily activities, the real load scenarios that a knee joint undergoes are more complex. In particular, this work did not consider the Varus-Valgus movements that often result in a higher amount of load on the medial compartment than the lateral one. In addition, the magnitude of contact forces varies between ordinary activities and the phase of activity, thus resulting in a complex relationship between the flexion angle, the maximum joint load and the balance of medial to lateral load distribution for different activities. Another aspect that requires further investigation is the sensitivity of the results, e.g. the amount of interface micromotion, to variations in bulk material properties, bone properties, loading conditions and the contact model used at the bone-implant interface.

5.   Conclusion

This study describes the computational design and numerical assessment of a stemmed tibial component with a fully porous stem with tuned tetrahedron lattice architecture. Although the results show an opportunity to improve the clinical performance of the current tibial implants, further experimental and numerical studies are required to validate the clinical applicability of the proposed design. The implant porosity has been optimally tailored to mitigate postoperative bone resorption and end-of-stem pain while satisfying the strength requirement necessary to sustain cyclic loadings. The mechanical properties of the implant are optimally tuned to bring about a concomitant reduction of bone resorption and interface micromotion. The numerical results suggest that the proposed concept could lead to a reduction of 17μm and 21μm in micromotion at the tip of the stem during gait cycle and deep knee bend, respectively. Clinically, this would be expected to alleviate the problem of end-of-stem pain that is not uncommon after total knee arthroplasty. In addition, the numerical results suggest a reduction in bone resorption of 26 % with respect to an identical tibial knee implant made of solid materials. This level of performance would translate in decreased periprosthetic fractures and enhanced bone stock at the time of revision surgery.

Appendix A: Assigning bone material properties using computed tomography (CT) data

The heterogeneous material properties of the tibia are captured through computed tomography (CT) data obtained from a 38 year old male , provided by the Visible Human project (United States National Library of Medicine, Bethesda, MD). The radiographic density of the CT images quantified as Hounsfield Unit (HU) is used to calculate the local properties of the tibia. Since the relationship between the HU and bone density is monotonic, a linear relationship between the bone apparent density and the HU is adopted as shown in Figure [40]. The bone apparent density represents the density of solid bone excluding the density of the fluid mass, namely the density of blood. On the other hand, the bone effective density accounts for the fluid mass. At regions where there is no bone, the effective density would be about 1024 kg/m3, which represents the density of blood. However at these regions, the apparent density and the HU value are zero.

To obtain the mechanical properties of the tibia, the apparent density for each element of the finite element model is determined from the HU value measured from the CT data ranging from 0 HU to 1567 HU. This ensures that the density of the fluid has no contribution to the mechanical properties of the tibia. The maximum value of HU corresponds to the densest region of the cortical bone with an apparent density of 2000 kg/m^3. The Young modulus of the tibia is then obtained using the relation

$$\begin{cases} E = 1904\,\rho^{1.64} & \rho < 0.95 \\ E = 2065\,\rho^{3.09} & 0.95 < \rho \end{cases} \quad,\quad v = 0.3 \tag{A.1}$$

where E is the elastic modulus of bone, and v is its Poisson's ratio. The properties are assumed to be isotropic, a simplification that does not lead to a considerable difference from the results that consider bone as orthotropic [39, 40]. This assumption contributes also to reduce the computational cost.

Appendix B: Filter density function

Early formulations of topology optimization problems generally yield instabilities in the optimal solutions that in turn affect result accuracy. A continuous density distribution is an asset for the implant strength while a discontinuous density distribution in the implant microstructure leads to stress concentration and compromise the implant strength thus increasing the probability of local failure. To avoid binary results (black and white patterns) for the density distribution, we use the following filter density function [72], to obtain the mechanical properties of each finite element mesh:

$$\tilde{x}_i = \frac{\sum_{j \in N_i} H_{ij} v_j x_j}{\sum_{j \in N_i} H_{ij} v_j} \tag{B.1}$$

wherein, N_i corresponds to neighborhood elements of element i, with volume of v_i.

H_{ij} is a weight factor matrix determined as follows:

$$H_{ij} = R - dist(i,j) \tag{B.2}$$

where R is the size of the neighbourhood that is referred to the filter size and $dist(i,j)$ is the distance between the element i and the center of the element j. The neighborhood of an element is defined as

$$N_i = \{j : dist(i,j) \leq R\} \tag{B.3}$$

Appendix C: Derivation of the stiffness tensor for the implant internal microstructure

To compute the sensitivity of the strain energy of the implant microstructure, as described in section 3.1, the derivative of the stiffness tensor is required for the entire implant. We use here a direct stiffness approach to find the global stiffness tensor, where the implant is discretized into small elements, and the elastic tensor of each element is calculated before the global stiffness matrix, K, assembly, where K is expressed as

$$K = \int_\Omega B_i^T D_i B_i \, dV \tag{C.1}$$

B is the strain-displacement matrix and D is the elastic tensor of element i, and Ω is the total volume of the implant. Since the strain-displacement matrix is independent of the design variables, the derivation of the stiffness matrix with respect to the design variables (relative density of each element) can be expressed as follows:

$$\frac{\partial K}{\partial x_i} = \int_\Omega B_i^T \frac{\partial D_i}{\partial x_i} B_i \, dV \tag{C.2}$$

Each mesh element corresponds to a tetrahedron-based cell that has three planes of symmetry; therefore 9 elastic constants are needed in the constitutive equations: 3 Young's moduli E_x, E_y, E_z, 3 Poisson's ratios v_{yz}, v_{zx}, v_{xy} and 3 shear moduli G_{yz}, G_{zx}, G_{yx}. The stiffness matrix of the unit cell can thus be expressed as

$$D = \begin{bmatrix} \dfrac{1 - v_{yz} v_{zy}}{E_y E_z \Delta} & \dfrac{v_{yx} + v_{zx} v_{yz}}{E_y E_z \Delta} & \dfrac{v_{zx} + v_{yx} v_{zy}}{E_y E_z \Delta} & 0 & 0 & 0 \\[2mm] \dfrac{v_{xy} + v_{xz} v_{zy}}{E_z E_x \Delta} & \dfrac{1 - v_{zx} v_{xz}}{E_z E_x \Delta} & \dfrac{v_{zy} - v_{zx} v_{xy}}{E_z E_x \Delta} & 0 & 0 & 0 \\[2mm] \dfrac{v_{xz} + v_{xy} v_{yz}}{E_x E_y \Delta} & \dfrac{v_{yz} + v_{xz} v_{yx}}{E_x E_y \Delta} & \dfrac{1 - v_{xy} v_{yx}}{E_x E_y \Delta} & 0 & 0 & 0 \\[2mm] 0 & 0 & 0 & 2G_{yz} & 0 & 0 \\[2mm] 0 & 0 & 0 & 0 & 2G_{zx} & 0 \\[2mm] 0 & 0 & 0 & 0 & 0 & 2G_{yx} \end{bmatrix} \tag{C.3}$$

$$\Delta = \frac{1 - v_{xy} v_{yx} - v_{yz} v_{zy} - v_{zx} v_{xz} - 2 v_{yz} v_{zx} v_{xy}}{E_x E_y E_z}$$

Since AH is used to obtain the elastic constants of the unit cell across a range of relative densities, with results shown in Figure 4, we can represent the elastic tensor of each element as a function of the element relative density and then use it to evaluate the derivative of the elastic tensor with respect to the design variables. The strain-displacement matrix is also derived by differentiating the displacements expressed through shape functions and nodal displacements. A 10 nodes isoparametric tetrahedron element is used to mesh the FE model of the implanted tibia. Hence, the strain-displacement matrix can be written as

$$B = [B_1 \quad B_2 \quad B_3 \quad B_4 \quad B_5 \quad B_6 \quad B_7 \quad B_8 \quad B_9 \quad B_{10}] \tag{C.4}$$

With

$$
B_k = \begin{bmatrix} N_{k,x} & 0 & 0 \\ 0 & N_{k,y} & 0 \\ 0 & 0 & N_{k,z} \\ N_{k,y} & N_{k,x} & 0 \\ 0 & N_{k,z} & N_{k,y} \\ N_{k,z} & 0 & N_{k,x} \end{bmatrix} \qquad k \in (1, 2, ..., 10) \tag{C.5}
$$

where $N_{k,x}$, $N_{k,y}$ and $N_{k,z}$ are the derivative of the shape functions with respect to the global coordinate system. The shape functions of a tetrahedron element with respect to the isoparametric coordinate system given by r, s and t (see figure below) can be defined as

$$
\begin{aligned}
N_1 &= 2s^2 - s \\
N_2 &= 2t^2 - t \\
N_3 &= 2r^2 - r \\
N_4 &= 2r^2 + 4rs + 4rt - 3r + 2s^2 + 4st - 3s + 2t^2 - 3t + 1 \\
N_5 &= 4st \\
N_6 &= 4rt \\
N_7 &= 4rs \\
N_8 &= 4s - 4rs - 4st - 4s^2 \\
N_9 &= 4t - 4rt - 4st - 4t^2 \\
N_{10} &= 4r - 4rs - 4rt - 4r^2
\end{aligned}
\tag{C.6}
$$
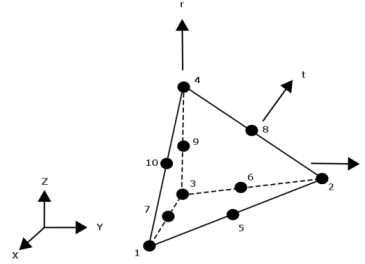
To construct the strain-displacement matrix, the derivative of the shape functions with respect to the generalized coordinate system is computed via the chain rule as

$$
\frac{\partial N}{\partial r} = \frac{\partial N}{\partial x}\frac{\partial x}{\partial r} + \frac{\partial N}{\partial y}\frac{\partial y}{\partial r} + \frac{\partial N}{\partial z}\frac{\partial z}{\partial r} \tag{C.7a}
$$

$$
\frac{\partial N}{\partial s} = \frac{\partial N}{\partial x}\frac{\partial x}{\partial s} + \frac{\partial N}{\partial y}\frac{\partial y}{\partial s} + \frac{\partial N}{\partial z}\frac{\partial z}{\partial s} \tag{C.7b}
$$

$$
\frac{\partial N}{\partial t} = \frac{\partial N}{\partial x}\frac{\partial x}{\partial t} + \frac{\partial N}{\partial y}\frac{\partial y}{\partial t} + \frac{\partial N}{\partial z}\frac{\partial z}{\partial t} \tag{C.7c}
$$

Using (C.7) results in

$$\begin{bmatrix} \dfrac{\partial N_k}{\partial x} \\[2mm] \dfrac{\partial N_k}{\partial y} \\[2mm] \dfrac{\partial N_k}{\partial z} \end{bmatrix} = \begin{bmatrix} \dfrac{\partial x}{\partial r} & \dfrac{\partial y}{\partial r} & \dfrac{\partial z}{\partial r} \\[2mm] \dfrac{\partial x}{\partial s} & \dfrac{\partial y}{\partial s} & \dfrac{\partial z}{\partial s} \\[2mm] \dfrac{\partial x}{\partial t} & \dfrac{\partial y}{\partial t} & \dfrac{\partial z}{\partial t} \end{bmatrix} \begin{bmatrix} \dfrac{\partial N_k}{\partial r} \\[2mm] \dfrac{\partial N_k}{\partial s} \\[2mm] \dfrac{\partial N_k}{\partial t} \end{bmatrix} = [J] \begin{bmatrix} \dfrac{\partial N_k}{\partial r} \\[2mm] \dfrac{\partial N_k}{\partial s} \\[2mm] \dfrac{\partial N_k}{\partial t} \end{bmatrix} \tag{C.8}$$

where $[J]$ is the Jacobian matrix. From (C.8), the Jacobian matrix of a 10 nodes tetrahedron element may be expressed [57] as

$$\begin{bmatrix} \dfrac{\partial N_1}{\partial r} & \dfrac{\partial N_2}{\partial r} & \dfrac{\partial N_3}{\partial r} & \dfrac{\partial N_4}{\partial r} & \dfrac{\partial N_5}{\partial r} & \dfrac{\partial N_6}{\partial r} & \dfrac{\partial N_7}{\partial r} & \dfrac{\partial N_8}{\partial r} & \dfrac{\partial N_9}{\partial r} & \dfrac{\partial N_{10}}{\partial r} \\[2mm] \dfrac{\partial N_1}{\partial s} & \dfrac{\partial N_2}{\partial s} & \dfrac{\partial N_3}{\partial s} & \dfrac{\partial N_4}{\partial s} & \dfrac{\partial N_5}{\partial s} & \dfrac{\partial N_6}{\partial s} & \dfrac{\partial N_7}{\partial s} & \dfrac{\partial N_8}{\partial s} & \dfrac{\partial N_9}{\partial s} & \dfrac{\partial N_{10}}{\partial s} \\[2mm] \dfrac{\partial N_1}{\partial t} & \dfrac{\partial N_2}{\partial t} & \dfrac{\partial N_3}{\partial t} & \dfrac{\partial N_4}{\partial t} & \dfrac{\partial N_5}{\partial t} & \dfrac{\partial N_6}{\partial t} & \dfrac{\partial N_7}{\partial t} & \dfrac{\partial N_8}{\partial t} & \dfrac{\partial N_9}{\partial t} & \dfrac{\partial N_{10}}{\partial t} \end{bmatrix} \begin{bmatrix} x_1 & y_1 & z_1 \\ x_2 & y_2 & z_2 \\ x_3 & y_3 & z_3 \\ x_4 & y_4 & z_4 \\ x_5 & y_5 & z_5 \\ x_6 & y_6 & z_6 \\ x_7 & y_7 & z_7 \\ x_8 & y_8 & z_8 \\ x_9 & y_9 & z_9 \\ x_{10} & y_{10} & z_{10} \end{bmatrix} \tag{C.9}$$

where $\{(x_i, y_i, z_i) \mid i \in (1,2,...,10)\}$ are the coordinates of the element nodes. By substituting (C.8) into (C.5), the strain-displacement matrix is calculated. Once the strain-displacement matrix for each element is obtained, the gradient of the strain energy for the corresponding element is computed from (C.2). The sensitivity of the objective function $\dfrac{\partial c(\tilde{x})}{\partial \tilde{x}}$ is assembled by the element sensitivity $\dfrac{\partial c(\tilde{x})}{\partial \tilde{x}_i}$ to obtain the vector of strain energy differentiation for the whole implant microarchitecture. The sensitivity analysis is then implemented under the optimization scheme described in section 3.1, so as to seek the optimum density distribution of the implant.

Appendix D: Convergence plot of the topology optimization scheme

As described in section 3, a density-based topology optimization is used in this study to optimally tailor the density gradients of the implant. To ensure solution convergence, we resort to the optimality criteria methods [58], in particular here we use the standard optimality criterion based on the Lagrangian function that benefits from knowledge on the physics and mechanics of the problem [73]. This method requires the calculation of the derivative of the objective function along with the derivative of the design constraints to update the design variables based on the initial guess [73].

In this work, the derivative of the implant compliance - obtained as described in section 3 - is used with the standard optimality criterion to find the optimum density distribution. As per the initial guess, a uniform relative density of 0.5 is assigned to the implant and the total strain energy of the implant is calculated. The optimization continues until the difference between two successive iterations is below 1%. As shown in the figure below, the objective function converges within 31 iterations.

References

1. Carr, B.C. and T. Goswami, *Knee implants – Review of models and biomechanics*. Materials & Design, 2009. **30**(2): p. 398-413.
2. Mihalko, W.M. and L.A. Whiteside, *Stem pain after cementless revision total knee arthroplasty*. Journal of Surgical Orthopaedic Advances, 2015. **24**(2): p. 137-9.
3. Barrack, R.L., T. Stanley, M. Burt, and S. Hopkins, *The effect of stem design on end-of-stem pain in revision total knee arthroplasty*. Journal of Arthroplasty, 2004. **19**(7 Suppl 2): p. 119-24.
4. Jasty, M., W.J. Maloney, C.R. Bragdon, D.O. O'Connor, T. Haire, and W.H. Harris, *The initiation of failure in cemented femoral components of hip arthroplasties*. The Journal of Bone & Joint Surgery, 1991. **73**(4): p. 551-8.
5. Rakotomanana, L.R., P.F. Leyvraz, A. Curnier, J.J. Meister, and J.J. Livio, *Comparison of tibial fixations in total knee arthroplasty: an evaluation of stress distribution and interface micromotions*. The Knee, 1994. **1**(2): p. 91-99.
6. Glenn, J.C., S.N. Sokoloski, B.M. Damer, and J.M. Tabit, *Tibia pain at end of stem with stemmed revision total knee arthroplasty: treatment with cortical strut graft technique*. Journal of Arthroplasty, 2010. **25**(3): p. 497 e1-5.
7. Haas, S.B., J.N. Insall, W. Montgomery, 3rd, and R.E. Windsor, *Revision total knee arthroplasty with use of modular components with stems inserted without cement*. The Journal of Bone & Joint Surgery, 1995. **77**(11): p. 1700-7.
8. Barrack, R.L., C. Rorabeck, M. Burt, and J. Sawhney, *Pain at the end of the stem after revision total knee arthroplasty*. Clinical Orthopaedics and Related Research, 1999(367): p. 216-25.
9. Bahraminasab, M., B.B. Sahari, K.L. Edwards, F. Farahmand, and M. Arumugam, *Aseptic loosening of femoral components – Materials engineering and design considerations*. Materials & Design, 2013. **44**: p. 155-163.
10. Bahraminasab, M., B.B. Sahari, K.L. Edwards, F. Farahmand, T.S. Hong, M. Arumugam, and A. Jahan, *Multi-objective design optimization of functionally graded material for the femoral component of a total knee replacement*. Materials & Design, 2014. **53**: p. 159-173.
11. Completo, A., A. Rego, F. Fonseca, A. Ramos, C. Relvas, and J.A. Simões, *Biomechanical evaluation of proximal tibia behaviour with the use of femoral stems in revision TKA: An in vitro and finite element analysis*. Clinical Biomechanics, 2010. **25**(2): p. 159-165.
12. Greenwald, A.S. and C.S. Heim, *Mobile-bearing knee systems: ultra-high molecular weight polyethylene wear and design issues*. Instructional Course Lectures, 2005. **54**: p. 195-205.
13. McEwen, H.M., P.I. Barnett, C.J. Bell, R. Farrar, D.D. Auger, M.H. Stone, and J. Fisher, *The influence of design, materials and kinematics on the in vitro wear of total knee replacements*. Journal of Biomechanics, 2005. **38**(2): p. 357-65.
14. Completo, A., F. Fonseca, J.A. Simoes, A. Ramos, and C. Relvas, *A new press-fit stem concept to reduce the risk of end-of-stem pain at revision TKA: a pre-clinical study*. Knee, 2012. **19**(5): p. 537-42.
15. Van Lenthe, G.H., M.C. de Waal Malefijt, and R. Huiskes, *Stress shielding after total knee replacement may cause bone resorption in the distal femur*. Journal of Bone & Joint Surgery, 1997. **79**(1): p. 117-22.
16. Gefen, A., *Computational simulations of stress shielding and bone resorption around existing and computer-designed orthopaedic screws*. Medical and Biological Engineering and Computing, 2002. **40**(3): p. 311-322.
17. Huiskes, R.I.K., H. Weinans, and B. Van Rietbergen, *The Relationship Between Stress Shielding and Bone Resorption Around Total Hip Stems and the Effects of Flexible Materials*. Vol. 274. 1992. 124-34.
18. Shi, L., L. Shi, L. Wang, Y. Duan, W. Lei, Z. Wang, J. Li, X. Fan, X. Li, S. Li, and Z. Guo, *The Improved Biological Performance of a Novel Low Elastic Modulus Implant*. PLoS ONE, 2013. **8**(2): p. e55015.

19. Karlsson, K.H., H. Ylänen, and H. Aro, *Porous bone implants.* Ceramics International, 2000. **26**(8): p. 897-900.

20. Matassi, F., A. Botti, L. Sirleo, C. Carulli, and M. Innocenti, *Porous metal for orthopedics implants.* Clinical Cases in Mineral and Bone Metabolism, 2013. **10**(2): p. 111-115.

21. Arabnejad Khanoki, S. and D. Pasini, *Multiscale design and multiobjective optimization of orthopedic hip implants with functionally graded cellular material.* Journal of Biomechanical Engineering, 2012. **134**(3): p. 031004.

22. Arabnejad Khanoki, S. and D. Pasini, *Fatigue design of a mechanically biocompatible lattice for a proof-of-concept femoral stem.* Journal of the Mechanical Behavior of Biomedical Materials, 2013. **22**: p. 65-83.

23. Arabnejad Khanoki, S. and D. Pasini, *The Fatigue Design of a Bone Preserving Hip Implant With Functionally Graded Cellular Material.* Journal of Medical Devices, 2013. **7**(2): p. 020907-020907.

24. Arabnejad, S., B. Johnston, M. Tanzer, and D. Pasini, *Fully porous 3D printed titanium femoral stem to reduce stress-shielding following total hip arthroplasty.* Journal of Orthopaedic Research, 2017. **35 (8)**: p. 1774–1783.

25. Au, A.G., V. James Raso, A.B. Liggins, and A. Amirfazli, *Contribution of loading conditions and material properties to stress shielding near the tibial component of total knee replacements.* Journal of Biomechanics, 2007. **40**(6): p. 1410-6.

26. Enab, T.A., *A comparative study of the performance of metallic and FGM tibia tray components in total knee replacement joints.* Computational Materials Science, 2012. **53**(1): p. 94-100.

27. Bobyn, J.D., R.A. Poggie, J.J. Krygier, D.G. Lewallen, A.D. Hanssen, R.J. Lewis, A.S. Unger, T.J. O'Keefe, M.J. Christie, S. Nasser, J.E. Wood, S.D. Stulberg, and M. Tanzer, *Clinical validation of a structural porous tantalum biomaterial for adult reconstruction.* Journal of Bone & Joint Surgery, 2004. **86-A Suppl 2**: p. 123-9.

28. Paganias, C.G., G.A. Tsakotos, S.D. Koutsostathis, and G.A. Macheras, *Osseous integration in porous tantalum implants.* Indian Journal of Orthopaedics, 2012. **46**(5): p. 505-513.

29. Kuiper, J. and H.R. Huiskes, *Numerical optimization of hip-prosthetic stem material.* 1992, Books and Journals International: Swansea.

30. Kuiper, J.H. and R. Huiskes, *Mathematical optimization of elastic properties: application to cementless hip stem design.* Journal of Biomechanical Engineering 1997. **119**(2): p. 166-74.

31. Arabnejad, S., R. Burnett Johnston, J.A. Pura, B. Singh, M. Tanzer, and D. Pasini, *High-strength porous biomaterials for bone replacement: A strategy to assess the interplay between cell morphology, mechanical properties, bone ingrowth and manufacturing constraints.* Acta biomaterialia, 2016. **30**: p. 345-56.

32. Coelho, P.G., J.B. Cardoso, P.R. Fernandes, and H.C. Rodrigues, *Parallel computing techniques applied to the simultaneous design of structure and material.* Advances in Engineering Software, 2011. **42**(5): p. 219-227.

33. Coelho, P.G., P.R. Fernandes, J.M. Guedes, and H.C. Rodrigues, *A hierarchical model for concurrent material and topology optimisation of three-dimensional structures.* Structural and Multidisciplinary Optimization, 2008. **35**(2): p. 107-115.

34. Fang, Z., B. Starly, and W. Sun, *Computer-aided characterization for effective mechanical properties of porous tissue scaffolds.* Computer-Aided Design, 2005. **37**(1): p. 65-72.

35. Guedes, J. and N. Kikuchi, *Preprocessing and postprocessing for materials based on the homogenization method with adaptive finite element methods.* Computer Methods in Applied Mechanics and Engineering, 1990. **83**(2): p. 143-198.

36. Hassani, B. and E. Hinton, *A review of homogenization and topology optimization I—homogenization theory for media with periodic structure.* Computers & Structures, 1998. **69**(6): p. 707-717.

37. Hassani, B. and E. Hinton, *A Review of Homogenization and Topology Opimization I I-Analytical and Numerical Solution of Homogenization Equations.* Journal of Computers & Structures, 1998. **69(6)**: p. 719-738.

38. Zienkiewicz, O.C. and R.L. Taylor, in *The Finite Element Method for Solid and Structural Mechanics (Sixth Edition).* 2005, Butterworth-Heinemann: Oxford. p. i.

39. Baca, V., Z. Horak, P. Mikulenka, and V. Dzupa, *Comparison of an inhomogeneous orthotropic and isotropic material models used for FE analyses.* Medical Engineering & Physics, 2008. **30**(7): p. 924-930.

40. Peng, L., J. Bai, X. Zeng, and Y. Zhou, *Comparison of isotropic and orthotropic material property assignments on femoral finite element models under two loading conditions.* Journal of Medical Engineering & Physics, 2006. **28**(3): p. 227-33.

41. Austman, R.L., J.S. Milner, D.W. Holdsworth, and C.E. Dunning, *The effect of the density–modulus relationship selected to apply material properties in a finite element model of long bone.* Journal of Biomechanics, 2008. **41**(15): p. 3171-3176.

42. Peng, L., J. Bai, X. Zeng, and Y. Zhou, *Comparison of isotropic and orthotropic material property assignments on femoral finite element models under two loading conditions.* Medical Engineering & Physics, 2006. **28**(3): p. 227-233.

43. Viceconti, M., R. Muccini, M. Bernakiewicz, M. Baleani, and L. Cristofolini, *Large-sliding contact elements accurately predict levels of bone-implant micromotion relevant to osseointegration.* Journal of Biomechanics, 2000. **33**(12): p. 1611-8.

44. Hipp, J.A., J.B. Brunski, M.S. Shephard, and G.V.B. Cochran, *Finite element model of implants in bone: interfacial assumptions.* Rensselaer Polytechnic Institute, Troy, NY, U.S.A.

45. Bergmann, G., A. Bender, F. Graichen, J. Dymke, A. Rohlmann, A. Trepczynski, M.O. Heller, and I. Kutzner, *Standardized Loads Acting in Knee Implants.* PLoS ONE, 2014. **9**(1): p. e86035.

46. Heinlein, B., I. Kutzner, F. Graichen, A. Bender, A. Rohlmann, A.M. Halder, A. Beier, and G. Bergmann, *ESB Clinical Biomechanics Award 2008: Complete data of total knee replacement loading for level walking and stair climbing measured in vivo with a follow-up of 6-10 months.* Clin Biomech (Bristol, Avon), 2009. **24**(4): p. 315-26.

47. Kutzner, I., B. Heinlein, F. Graichen, A. Bender, A. Rohlmann, A. Halder, A. Beier, and G. Bergmann, *Loading of the knee joint during activities of daily living measured in vivo in five subjects.* Journal of Biomechanics, 2010. **43**(11): p. 2164-73.

48. Arabnejad, S. and D. Pasini, *Mechanical properties of lattice materials via asymptotic homogenization and comparison with alternative homogenization methods.* International Journal of Mechanical Sciences, 2013. **77**: p. 249-262.

49. Masoumi Khalil Abad, E., S. Arabnejad Khanoki, and D. Pasini, *Fatigue design of lattice materials via computational mechanics: Application to lattices with smooth transitions in cell geometry.* International Journal of Fatigue, 2013. **47**: p. 126-136.

50. Hollister, S.J. and N. Kikuchi, *A comparison of homogenization and standard mechanics analyses for periodic porous composites.* Computational Mechanics, 1992. **10**(2): p. 73-95.

51. Hassani, B., *A direct method to derive the boundary conditions of the homogenization equation for symmetric cells.* Communications in Numerical Methods in Engineering, 1996. **12**(3): p. 185-196.

52. Parthasarathy, J., B. Starly, S. Raman, and A. Christensen, *Mechanical evaluation of porous titanium (Ti6Al4V) structures with electron beam melting (EBM).* Journal of the Mechanical Behavior of Biomedical Materials, 2010. **3**(3): p. 249-259.

53. Wycisk E, E.C., Siddique S, Walter L. F., *High cycle fatigue (HCF) performance of Ti-6Al- 4V alloy processed by selective laser melting.* Advanced Materials Research: Trans Tech Publ, 2013: p. 134-139.

54. Liu, K. and A. Tovar, *An efficient 3D topology optimization code written in Matlab.* Structural and Multidisciplinary Optimization, 2014. **50**(6): p. 1175-1196.

55. Zhou, M. and G.I.N. Rozvany, *Second World Congress on Computational Mechanics The COC algorithm, Part II: Topological, geometrical and generalized shape optimization.* Computer Methods in Applied Mechanics and Engineering, 1991. **89**(1): p. 309-336.

56. Ridzwan M, S.S., Hassan A, Shokri A, Ibrahim MM, *Problem of stress shielding and improvement to the hip implant designs: a review.* Journal of Medical Science, 2007. **7**: p. 460-467.

57. Logan, D.L., *A First Course in the Finite Element Method Using Algor*. 2000: Brooks/Cole Publishing Co. 864.

58. Bendsøe, M., *Optimization of structural topology shape and material*, Springer, Editor. 1995: New York.

59. ASTM F1800-12, *Standard Practice for Cyclic Fatigue Testing of Metal Tibial Tray Components of Total Knee Joint Replacements*. 2012, West Conshohocken, PA.

60. Small, S.R., R.D. Rogge, R.A. Malinzak, E.M. Reyes, P.L. Cook, K.A. Farley, and M.A. Ritter, *Micromotion at the tibial plateau in primary and revision total knee arthroplasty: fixed versus rotating platform designs.* Bone & Joint Research, 2016. **5**(4): p. 122-129.

61. Conlisk, N., H. Gray, P. Pankaj, and C.R. Howie, *The influence of stem length and fixation on initial femoral component stability in revision total knee replacement.* Bone & Joint Research, 2012. **1**(11): p. 281-288.

62. Ebrahimi, H., M. Rabinovich, V. Vuleta, D. Zalcman, S. Shah, A. Dubov, K. Roy, F.S. Siddiqui, H.S. E, H. Bougherara, and R. Zdero, *Biomechanical properties of an intact, injured, repaired, and healed femur: an experimental and computational study.* Journal of the Mechanical Behavior of Biomedical Materials, 2012. **16**: p. 121-35.

63. Melancon, D., Z.S. Bagheri, R.B. Johnston, L. Liu, M. Tanzer, and D. Pasini, *Mechanical characterization of structurally porous biomaterials built via additive manufacturing: experiments, predictive models, and design maps for load-bearing bone replacement implants.* Acta biomaterialia, 2017.

64. Konda Gokuldoss, P., S. Kolla, and J. Eckert, *Additive Manufacturing Processes: Selective Laser Melting, Electron Beam Melting and Binder Jetting—Selection Guidelines.* Materials, 2017. **10**(6): p. 672.

65. Vaezi, M., S. Chianrabutra, B. Mellor, and S. Yang, *Multiple material additive manufacturing – Part 1: a review.* Virtual and Physical Prototyping, 2013. **8**(1): p. 19-50.

66. Balla, V.K., S. Bodhak, S. Bose, and A. Bandyopadhyay, *Porous Tantalum Structures for Bone Implants: Fabrication, Mechanical and In vitro Biological Properties.* Acta biomaterialia, 2010. **6**(8): p. 3349-3359.

67. Moiduddin, K., S. Darwish, A. Al-Ahmari, S. ElWatidy, A. Mohammad, and W. Ameen, *Structural and mechanical characterization of custom design cranial implant created using additive manufacturing.* Electronic Journal of Biotechnology, 2017. **29**(Supplement C): p. 22-31.

68. Tunchel, S., A. Blay, R. Kolerman, E. Mijiritsky, and J.A. Shibli, *3D Printing/Additive Manufacturing Single Titanium Dental Implants: A Prospective Multicenter Study with 3 Years of Follow-Up.* International Journal of Dentistry, 2016. **2016**: p. 8590971.

69. Liu, L., P. Kamm, F. García-Moreno, J. Banhart, and D. Pasini, *Elastic and failure response of imperfect three-dimensional metallic lattices: the role of geometric defects induced by Selective Laser Melting.* Journal of the Mechanics and Physics of Solids, 2017. **107**: p. 160-184.

70. Sobral, J.M., S.G. Caridade, R.A. Sousa, J.F. Mano, and R.L. Reis, *Three-dimensional plotted scaffolds with controlled pore size gradients: Effect of scaffold geometry on mechanical performance and cell seeding efficiency.* Acta biomaterialia, 2011. **7**(3): p. 1009-18.

71. Khoda, A.K., I.T. Ozbolat, and B. Koc, *Engineered tissue scaffolds with variational porous architecture.* Journal of Biomechanical Engineering 2011. **133**(1): p. 011001.

72. Sigmund, O. and J. Petersson, *Numerical instabilities in topology optimization: A survey on procedures dealing with checkerboards, mesh-dependencies and local minima.* Structural optimization, 1998. **16**(1): p. 68-75.

73.   Avinash Shukla, A.M., *Review of optimality criterion approach scope, limitation and development in topology optimization.* International Journal of Advances in Engineering & Technology, 2013. **Vol. 6**(Issue 4): p. 1886-1889.

74.   Chong, D.Y., U.N. Hansen, and A.A. Amis, *Analysis of bone-prosthesis interface micromotion for cementless tibial prosthesis fixation and the influence of loading conditions.* Journal of Biomechanics, 2010. **43**(6): p. 1074-80.
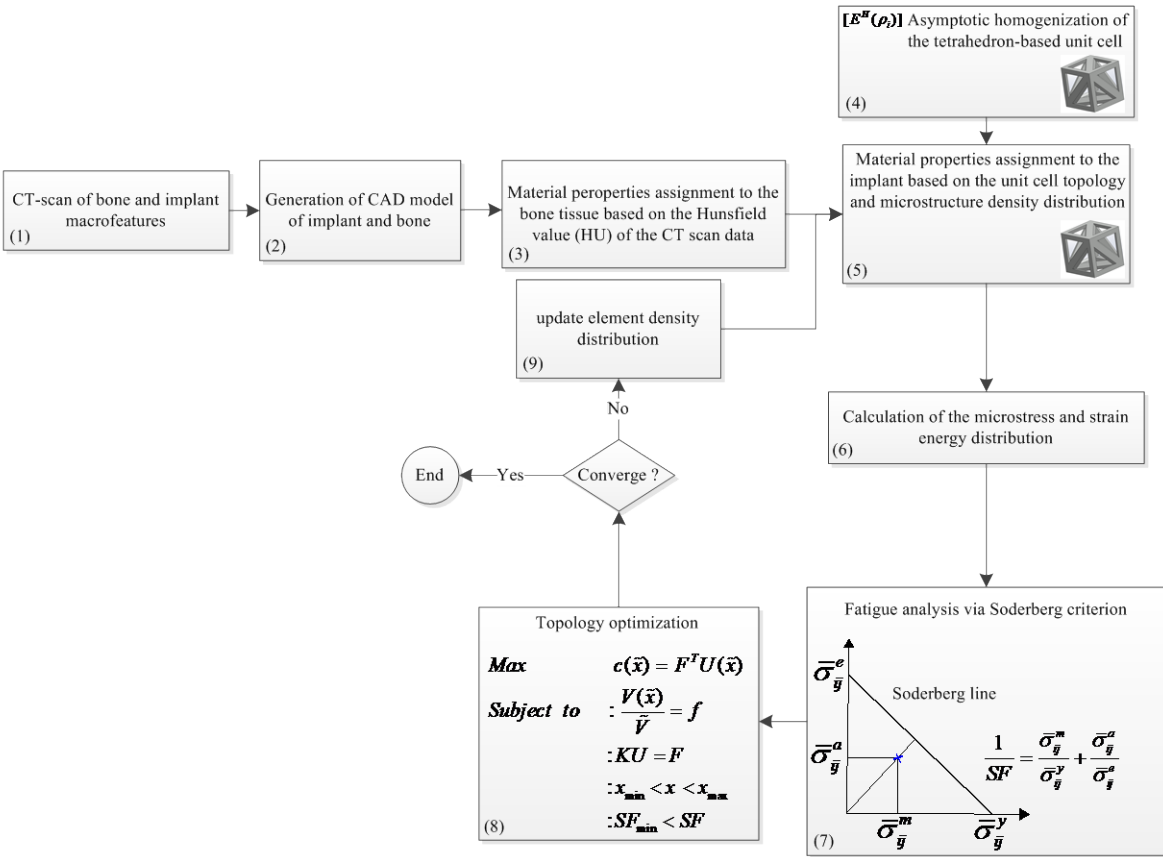
Figure 1

Figures

Figure 1: Flow chart illustrating the analysis and design scheme used to develop a graded cellular knee implant minimizing bone resorption and interface micromotion. Legend: mean stress: $\bar{\sigma}_{ij}^{m}$, alternating stress: $\bar{\sigma}_{ij}^{a}$, yield stress of tetrahedron cell unit: $\bar{\sigma}_{ij}^{y}$, fatigue strength of tetrahedron cell unit: $\bar{\sigma}_{ij}^{e}$, implant compliance: c, relative density of tetrahedron cell unit: ρ, minimum element density: ρ_{min}, maximum element density: ρ_{max}, displacement vector: U, stiffness matrix of tetrahedron unit cell: K_i, volume constraint: f, predefined volume of the implant: V_0, force vector: F, implant safety factor: SF, minimum allowable safety factor: SF_{min}.

Figure 2

(a)　　　　(b)　　　　(c)　　　　(d)
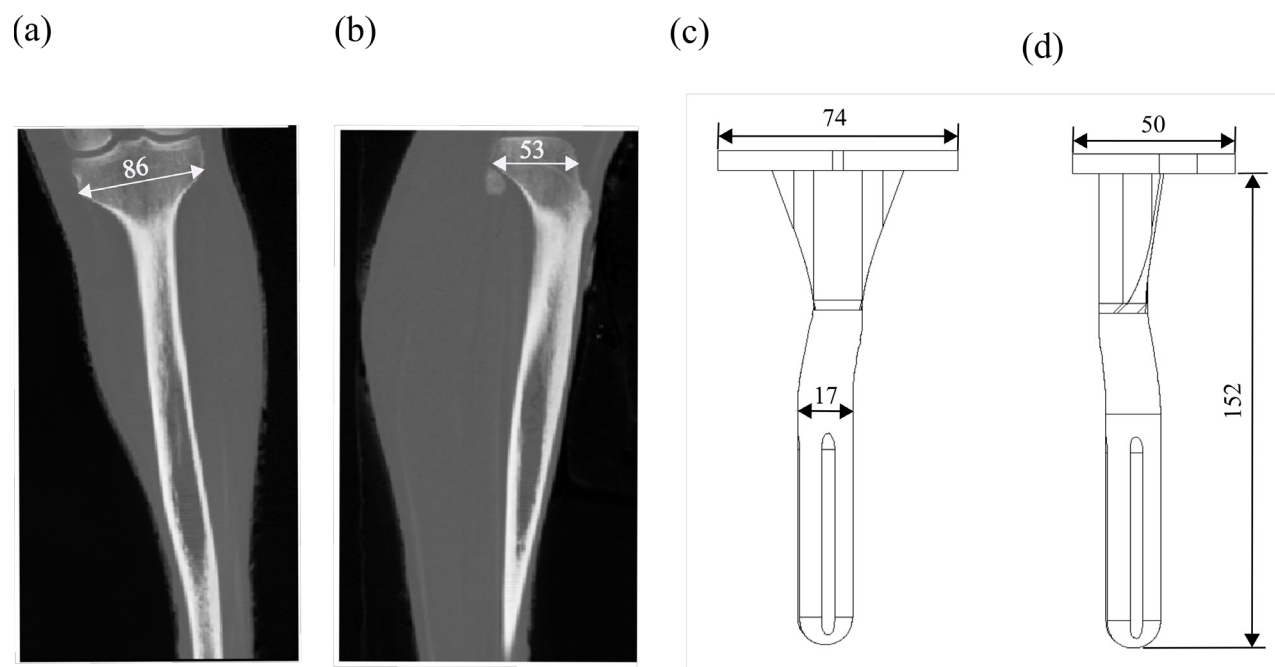
Figure 2: CT scan data used to create the solid model of the tibia along with the dimensions of the tibia and tibial knee implant in mm. Frontal view of the tibia (a), sagittal view of the tibia (b), Frontal view of the implant (c), sagittal view of the implant (c).

Figure 3
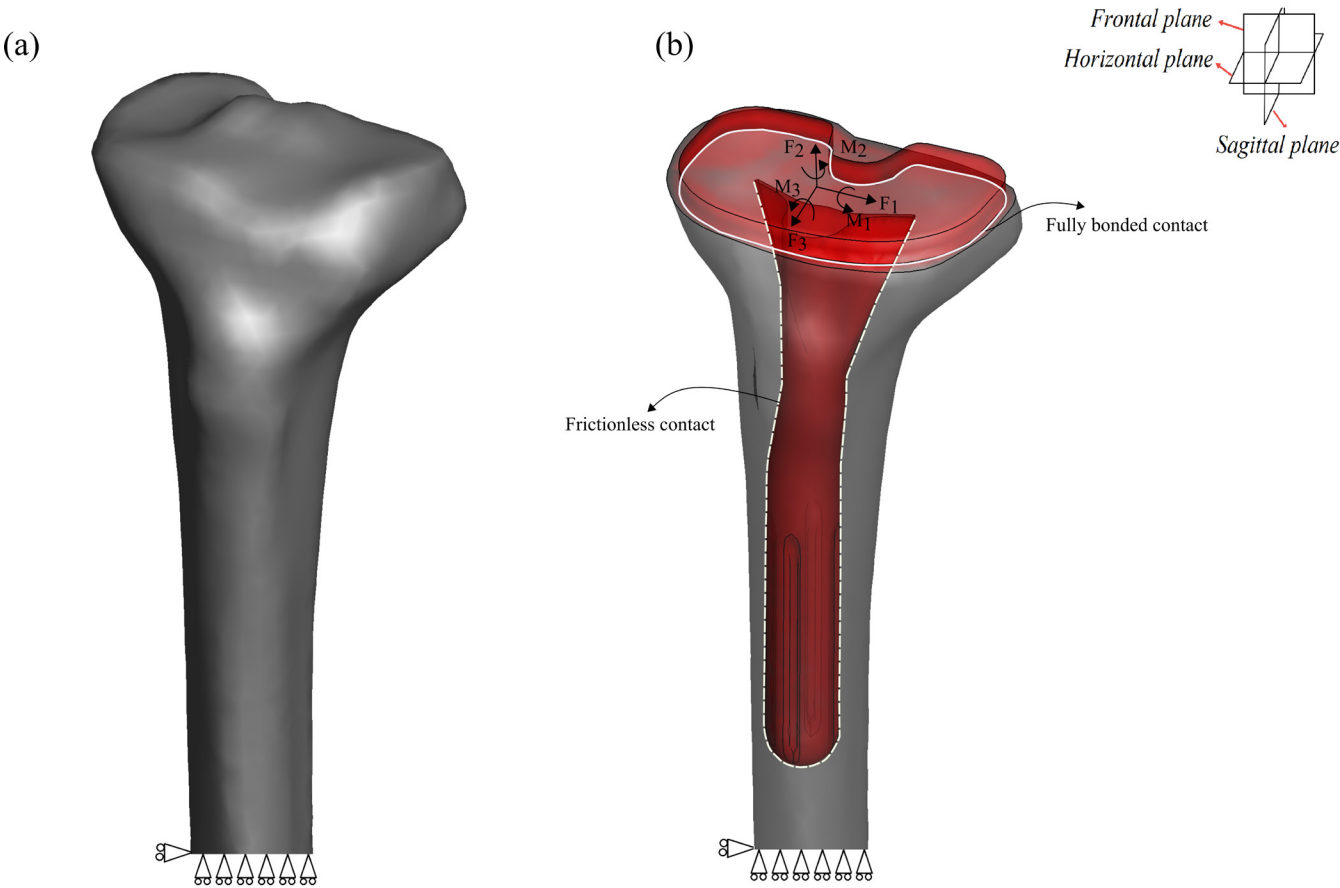
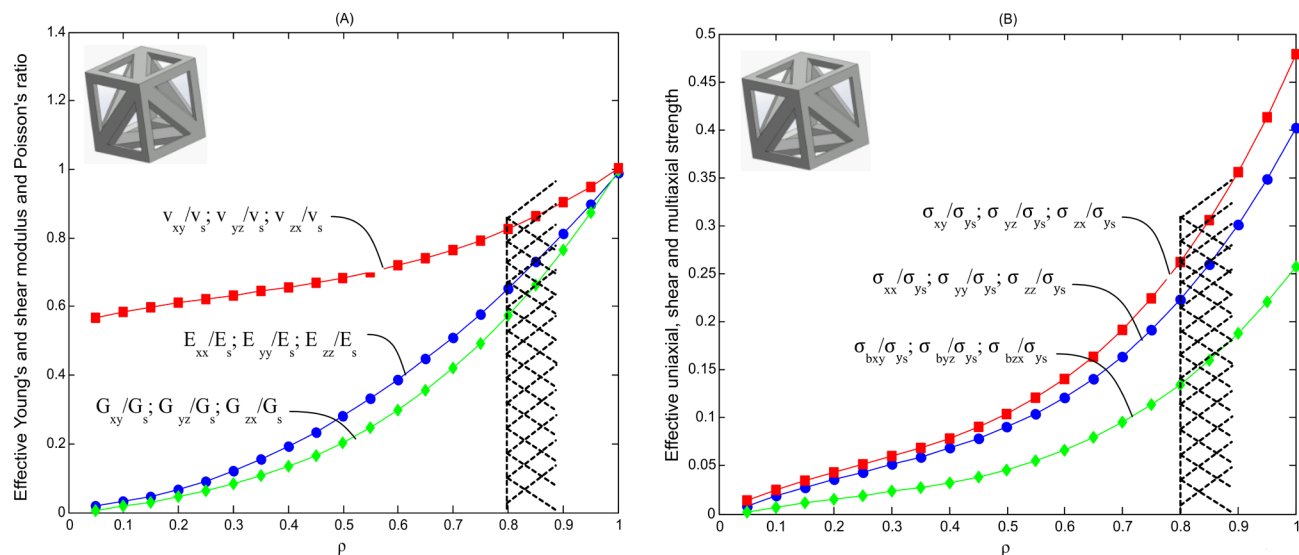Figure 3: 3D finite element model of the intact tibiae (a), and implanted prosthesis (b).

Figure 4

Figure 4: (A) Effective elastic and (B) effective strength properties of Tetrahedron based lattice as a function of relative density. Effective elastic properties and yield strengths normalized with respect to elastic properties and yield strengths of bulk material. Only three independent elastic constants are necessary for the tetrahedron-based cell which is orthotropic and has 3 planes of symmetry: (Young`s modulus), G_{xy} (Shear modulus) and v_{yz} (Poisson's ratio). σ_{xx}, σ_{xy} and σ_{bxy} refer to uniaxial, shear and biaxial strength respectively. Values of ρ above 0.8 are dismissed due to cell topology degeneration.
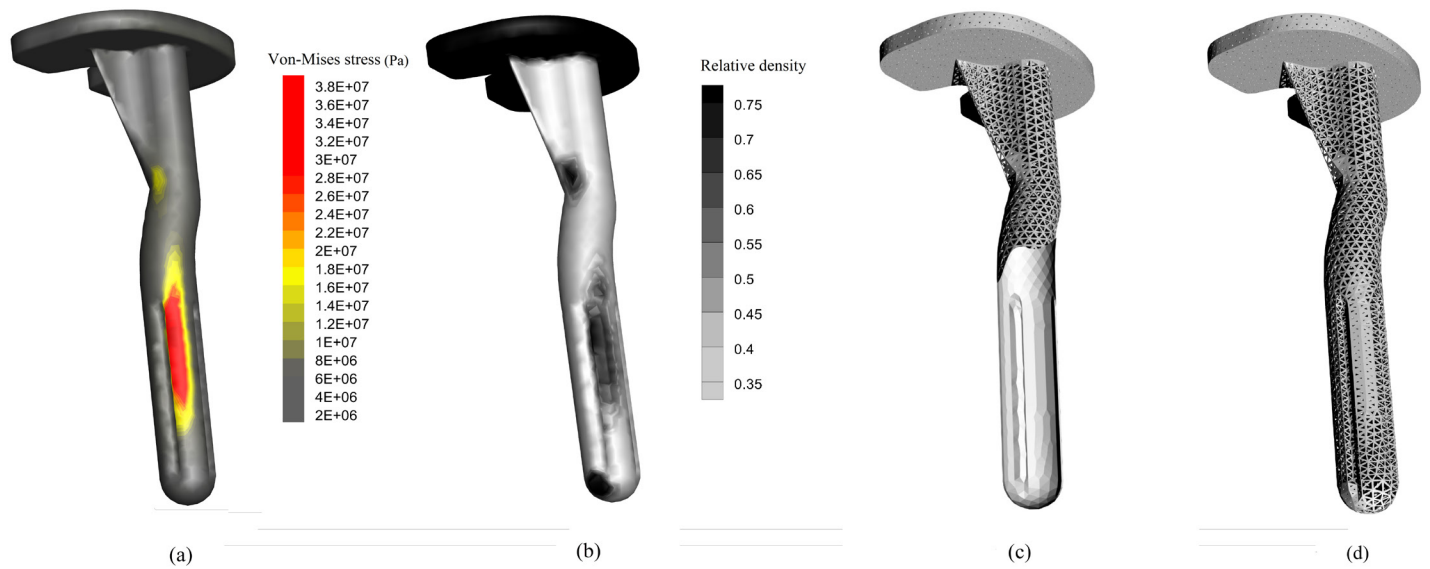
Figure 5

Figure 5: (a) Von-Mises stress distribution; (b) optimum relative density distribution to ensure adequate fatigue resistance against daily cyclic loads; (c) graded cellular implant with tailored porosity in the stem ranging 0.3-0.7. A thin solid exterior (shown only partially in the figure) coats the stem, a clinically recommended feature introduced to ease implant removal at the time of revision surgery; (d) internal architecture of the tibial implant, where the thin shell is here omitted for a global visualization of the whole internal microstructure.

Figure 6
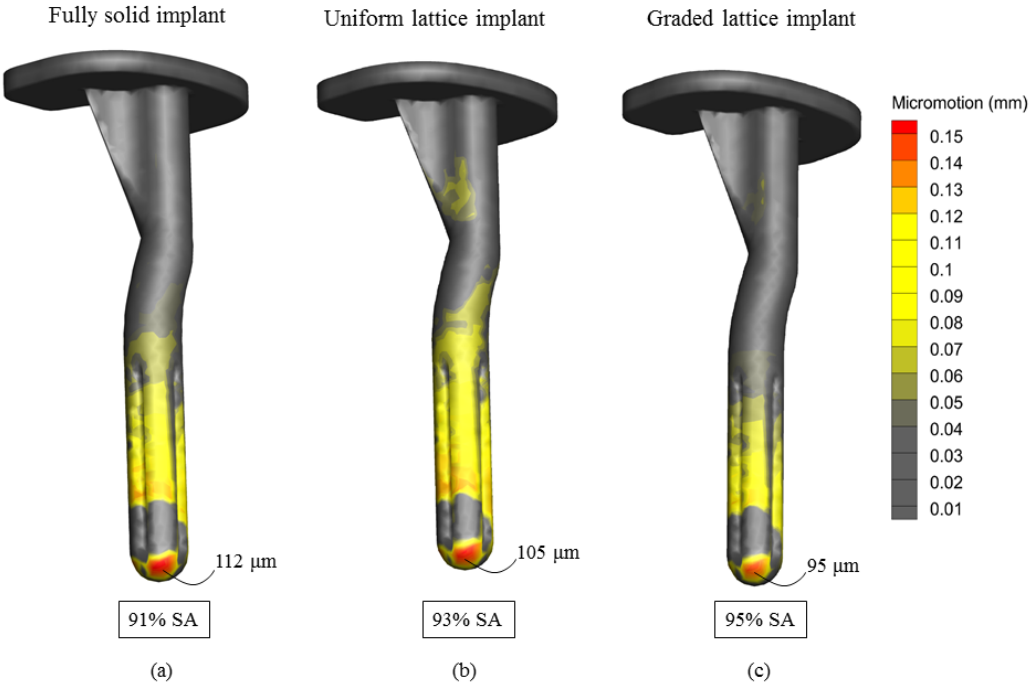
Figure 6: Interface micromotion distribution at 30% of gait cycle for a fully dense titanium implant (a), cellular implant with uniform relative density of 60% (b), and graded cellular implant (c). SA: surface area of the prosthesis [74].
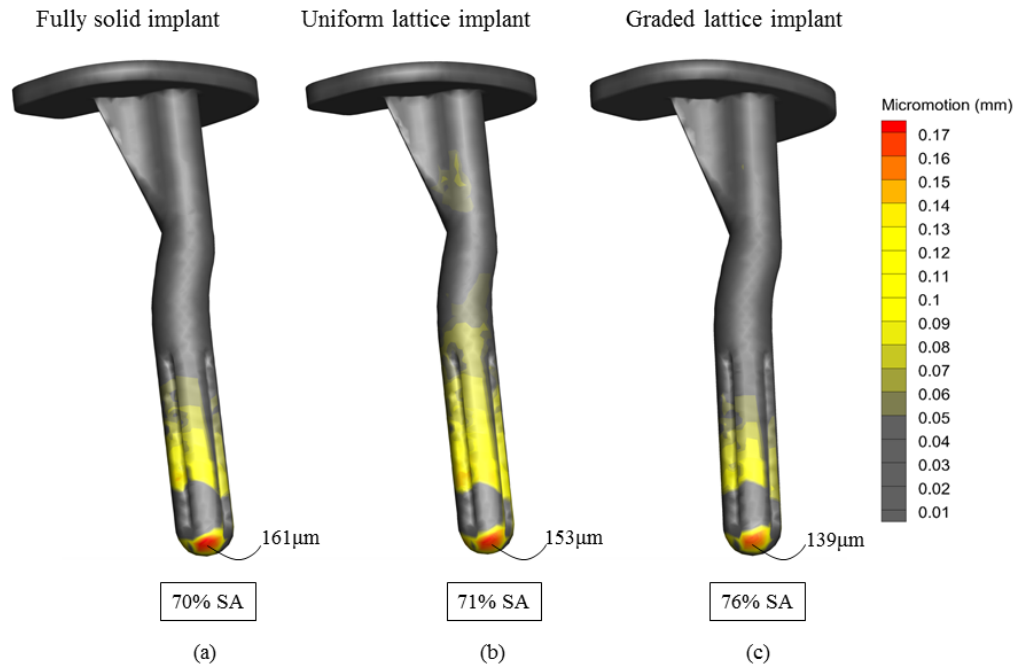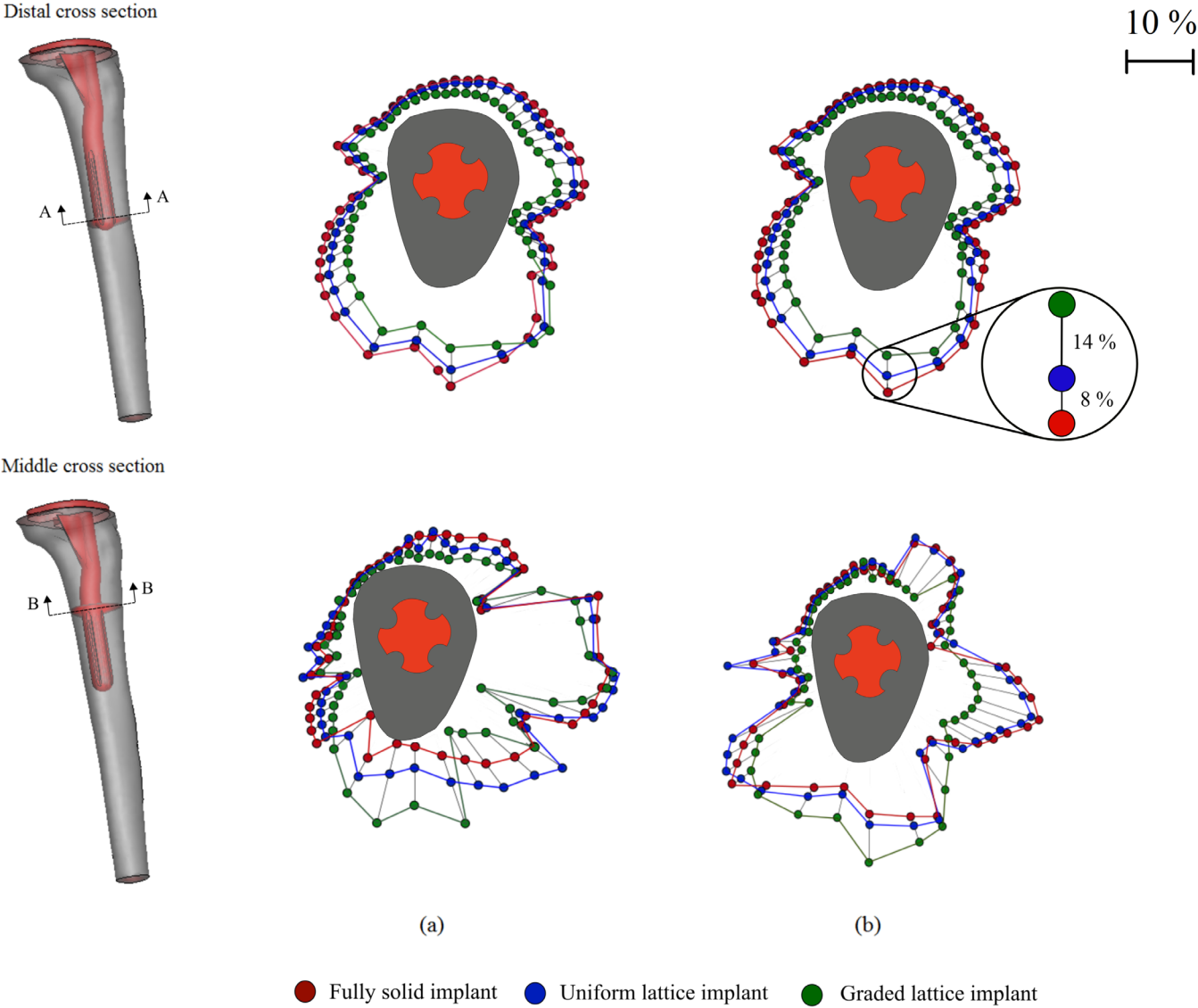
Figure 7

Figure 7: Interface micromotion distribution at deep bend for a fully dense titanium implant (a), cellular implant with uniform relative density of 60% (b), and a graded cellular implant (c). SA: surface area of the prosthesis [74].

Figure 8

Figure 8: Relative distribution of interface micromotion around the stem surface with respect to the fully solid implant. % values are shown at the distal and mid regions along the stem length for 30% of gait cycle (a), and deep bend (b).
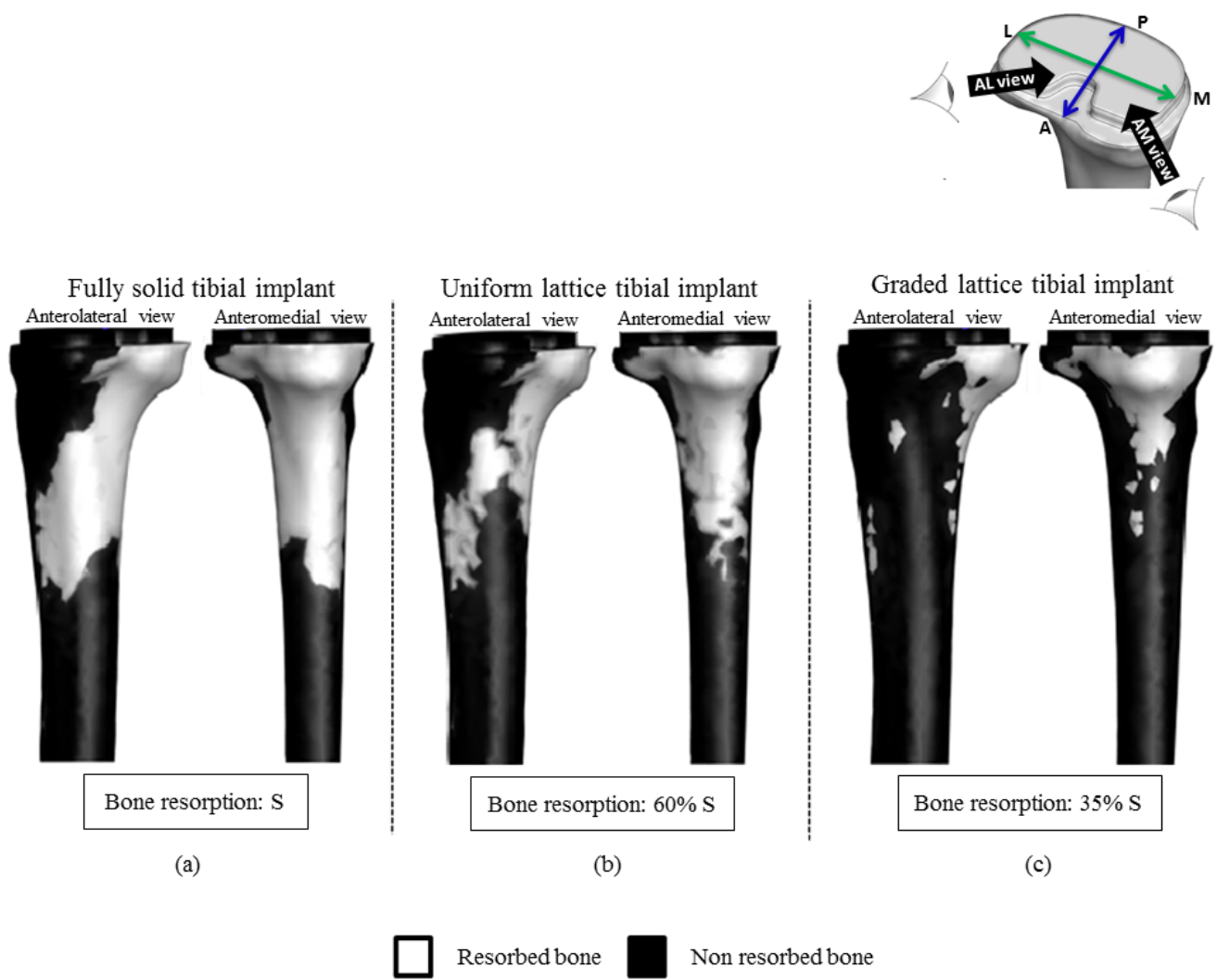
Figure 9

Figure 9: Distribution of bone resorption in knee prosthesis around (a) fully dense titanium implant; (b) cellular implant with uniform relative density of 60%; and (c) graded cellular implant. L: Lateral, M: Medial, A: Anterior, P: Posterior, AL: Anterolateral, AM: Anteromedial.
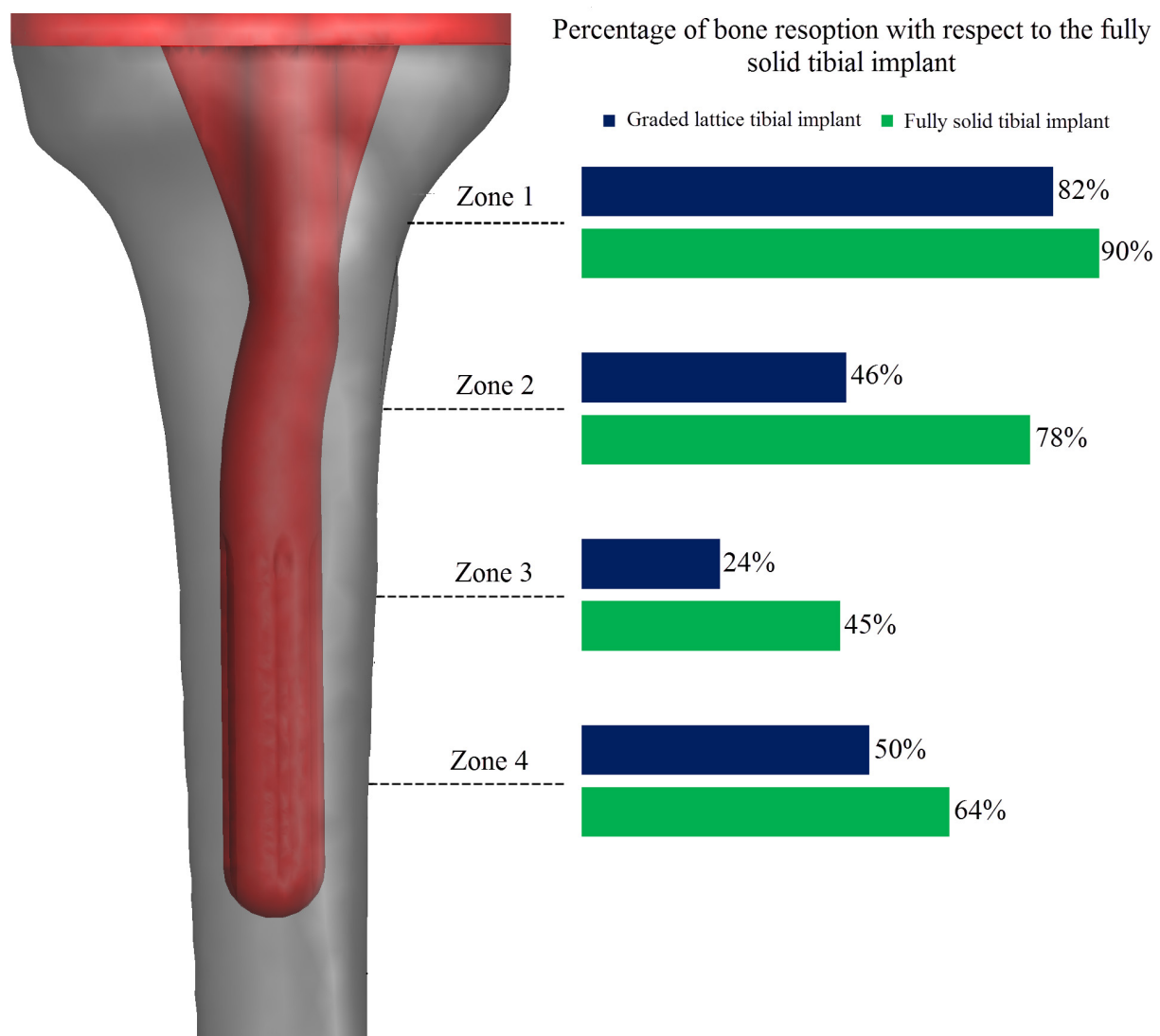
Figure 10

Figure 10: Percentage of bone resorption with respect to a fully solid tibial implant here taken as a baseline for (i) graded cellular implant, and (ii) uniform cellular implant with relative density of 0.6.
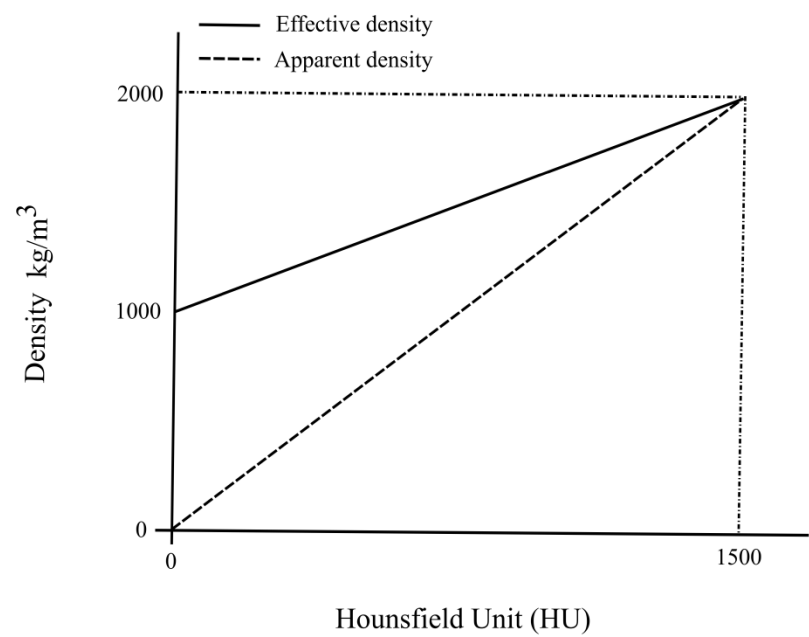
Figures in the Appendices

Figure A.1: Linear relationship between Hounsfield number and both effective density and apparent density.
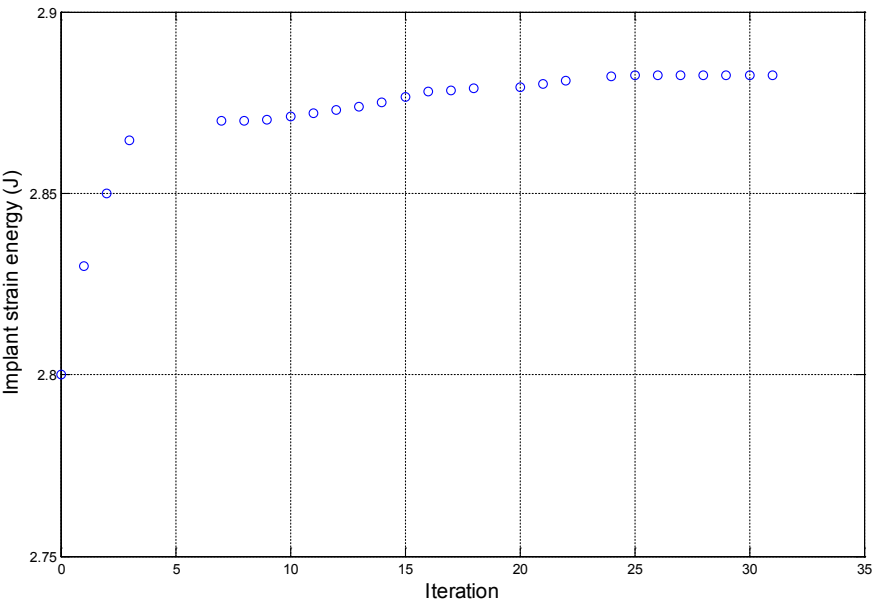
Figure D.1

Figure D.1: The convergence plot of the topology optimization scheme.

Table 1

Tables

	No.	Load case	Force/N			Moment/N.mm		
			F_1	F_2	F_3	M_1	M_2	M_3
	1	20% of gait cycle	-76.05	-318.9	-169.96	2420	-1900	3430
Level	2	30% of gait cycle	-144.65	-1442.14	52.79	3760	1090	-4790
walking	3	40% of gait cycle	-71.96	-2141.34	61.18	8850	1070	20220
Level	4	Deep knee bend	75.8	-2537.57	-8.3	13220	-2230	12030
bending								

Table.1 Loading values measured on an instrumented implant [47] and used in this study. F_1, F_2 and F_3 act in the medio-lateral, vertical and posterior-anterior directions respectively. M_1, M_2 and M_3 act in the sagittal, horizontal and frontal plane of the tibiae, as shown at the right top corner in Figure 3.